Molecular Engineering Using an Anthanthrone Dye for Low Cost Hole Transport Materials: A Strategy for Dopant Free, High Efficiency and Stable Perovskite Solar Cells

Hong Duc Pham,[a♦] Thu Trang Do,[a] Jinhyun Kim,[b] Cecile Charbonneau,[c] Sergei Manzhos,[d] Krishna Feron,[e, f] Wing Chung Tsoi,[c] James R. Durrant,[b,c] Sagar M. Jain,[c♦*] Prashant Sonar[a*]

[a]Institute of Future Environment and School of Chemistry, Physics and Mechanical Engineering, Queensland University of Technology (QUT), 2 George Street, Brisbane, QLD-4001, Australia

[b]Department of Chemistry and Centre for Plastic Electronics, Imperial College London, Exhibition Road, London SW7 2AZ, United Kingdom

[c]SPECIFIC, College of Engineering, Swansea University Bay Campus, Fabian Way, SA1 8EN Swansea, United Kingdom

[d]Department of Mechanical Engineering, Faculty of Engineering, National University of Singapore

[e]CSIRO Energy Centre, NSW-2304, Australia.

[f]Centre for Organic Electronics, University of Newcastle, Callaghan, NSW 2308, Australia

♦ These authors contributed equally to the work Corresponding author contact information

Prashant Sonar*, sonar.prashant@qut.edu.au

Sagar M. Jain*, s.m.jain@swansea.ac.uk

Abstract

In this report, we are presenting highly efficient and humidity-resistant perovskite solar cells (PSCs) using two new small molecule hole transporting materials (HTM) made from a cost-effective precursor anthanthrone (ANT) dye, namely ACE-ANT-ACE and TPA-ANT-TPA. We have systematically compared our newly developed HTMs with the conventional 2,2´,7,7´-tetrakis(N,N´-di-p-methoxyphenylamino)-9,9´-spirbiuorene (Spiro-OMeTAD). ACE-ANT-ACE and TPA-ANT-TPA were used as a dopant free HTMs in mesoscopic TiO_2/$CH_3NH_3PbI_3$/HTM solid-state PSCs, and the performance as well as stability were compared with Spiro-OMeTAD based PSCs. After extensive optimization of the metal oxide scaffold and device processing conditions, dopant-free novel TPA-ANT-TPA HTM based PSCs devices achieved a maximum PCE of 17.5% with negligible hysteresis. An impressive current of 21 mA/cm^2 obtained is also confirmed from photocurrent density with a higher fill factor of 0.79. The obtained PCE of 17.5% utilizing TPA-ANT-TPA is higher performance than the devices prepared using doped Spiro-OMeTAD (16.8%) as hole transport layer at 1 sun condition. It is found that doping of LiTFSI salt increases hygroscopic characteristics in Spiro-OMeTAD this leads to the fast degradation of solar cells. While, solar cells prepared using undoped TPA-ANT-TPA shows dewetting and improved stability. Additionally, the new HTMs form a fully homogeneous and completely covering thin film on the surface of the active light absorbing perovskite layers that acts as a protective coating for underlying perovskite films. This breakthrough paves the way for development of new inexpensive, more stable, and highly efficient ANT core based lower cost HTMs for cost effective conventional and printable PSCs.

Photovoltaic or solar cells are currently considered as the possible and suitable alternative for traditional non-conventional energy harvesting technology to tackle the issues of environmental pollution, climate change and potential future shortage of hydrocarbon-based energy supply. With the goal of making this alternative feasible, much research on various solar cell technologies has been performed. The main challenges include reducing the cost, increasing the power conversion efficiency (PCE) values, and improving stability to enable large-scale commercial manufacturing for public use. Apart from conventional high performance and stable silicon based inorganic solar cells,[1] dye sensitised solar cells (DSSC),[2] organic solar cells (OSCs)[3] and perovskite solar cells(PSCs)[4, 5] are some emerging technologies where the active light absorbing layer can be deposited on large scale using either pure organic or organic-inorganic solution processable light absorbing semiconducting layer. These technologies are becoming attractive options due to the potential for lower cost, optoelectronic tunability (energy levels and optical band gap), high efficiency and opportunities to scale them up in the form of flexible prototypes using roll to roll printing.[4, 6] Among various organic based light absorbing semiconductors, metal-free organic dyes are prospective candidates on account of their practical advantages, including high molar absorption coefficients, facile structure tuning, easy charge carrier mobility modulation, and simple and inexpensive syntheses.[7] The dye-based semiconductors have been employed successfully in various solar cell devices either as donors (p-type materials) or acceptors (n-type materials). Among various and numerous types of dyes, recently, some of the key dyes such as the dark red diketopyrrolopyrrole (DPP) and isoindigo (IS) have been widely used as a significant building blocks for designing and synthesizing high performance low band gap materials for organic and dye sensitized solar cells.[8] In addition to OSCs and DSSCs, recently, carbazole-based low cost dyes have been successfully used as hole-transporting materials (HTMs) in PSCs and an impressive PCE has been achieved.[9]

Recently, dibenzo[*def*,*mno*]chrysene (anthanthrene), one type of polycyclic aromatic hydrocarbons, has been used intensively as a versatile building block for designing advanced functional materials for organic field-effect transistors (OFETs), organic light emitting diodes (OLED) and organic solar cells (OSCs) devices, due to its outstanding properties.[10, 11, 12] The commercially available anthanthrene dye is not only cost-effective but also possesses a good environmental stability and provides good solubility. Among anthanthrene derivatives, 4,10-dibromoanthanthrone, named as VAT Orange 3 (Scheme 1), is a useful scaffold due to its various exciting features. Firstly, the conjugation backbone of the dye can be extended and its optoelectronic properties can be tuned easily via functionalization of any chemical moiety (either aliphatic or aromatic depending on requirements) at the possible 4, 10 and 6, 12 axes.[13-15] Secondly, the solution processibility aspect can be enhanced by introducing either longer straight or branched alkyl chains via the bromine atoms at the 4 and 10 positions or at the 6 and 12 positions via alkylation.[13] Thirdly, the possibilities of tuning the starting n-type material (due to two ketonic groups at 6 and 12) to p-type organic semiconductors by introducing electron donating groups.[14] In addition to the above features, the central fused aromatic six-membered rings in the centre deliver structural planarity leading to ordered morphology in thin films which is essential for better charge delocalization and transport.[12] Furthermore, this compound seems to be crystallized simply due to its symmetrical structure and can provide ample opportunities to vary the UV-visible absorption range based on rigid and extended π-conjugated backbone.[16] Although a handful of anthanthrone derivatives were used successfully in OFETs, OLED and OSCs, till date there are no reports using this cost-efficient dye and its derivatives as a hole transporting material in the fast moving PSCs technology.

In recent years, PSCs have gained enormous attention from both academia and industry due to their easy processibility, potentially lower cost and ability to reach the performance

close to the solar cell technologies currently used globally. The rapid development of this technology is almost comparable to common and traditional solar energy technologies, such as copper indium gallium selenide (CIGS), cadmium telluride (CdTe) and silicon. From the first initial PCE of 3.8% reported in 2009,[17] the power conversion efficiency (PCE) of PSCs has now reached 22.1%.[18] One of key points resulting in the rapid success is the presence of a hole-transporting layer (HTL) in the devices. This layer not only assists to transport the holes after exciton dissociation but also plays a significant role in controlling the stability, supressing charge recombination and preventing the perovskite layer from the invasion of the moisture/oxygen and electrode penetration.[19, 20] Earlier works showed that while the PCE of perovskite devices with a HTL has recorded greater than 20%,[21-23] the efficiency in the absence of this layer has been around 14%.[24] In terms of designing materials for the HTL, various inorganic,[25] small molecular,[26, 27] and polymeric[28] HTMs have been developed. Among them, small molecules are more attractive and can offer considerable benefits such as simplicity of purification, high purity, definite molecular weight, promising tunable highest occupied molecular orbital (HOMO) and lowest unoccupied molecular orbital (LUMO) energy levels and good batch-to-batch reproducibility.[29] Also, small molecular HTMs have been proven to be one of the best choices of materials till date compared to other type of HTMs. The 2, 2', 7, 7'-tetrakis-(*N*,*N*-di-*p*-methoxyphenylamine)-9,9'-spiro-bifluorene (Spiro-OMeTAD) has been recognized as one of the key candidates which has achieved the highest PCE close to 20.8% in PSCs.[21] However, the major drawback of Spiro-OMeTAD is that it gives such a high performance only in combination with some dopants, which are often vulnerable to moisture, and this critically determines the stability of solar cell devices.[26, 30] In addition, tedious synthesis and a cost too high for commercial use have impeded overall PSC development.[22, 26]

In order to replace Spiro-OMeTAD, researchers worldwide have been designing and developing alternative HTMs. Among them, the triphenylamine (TPA) based HTMs in combination with various different π-functional moieties have shown remarkable success due to simplicity in synthesis and promising PCE value upward growth.[31, 32-35] Thus, our group has designed HTMs by using anthanthrone dye as a starting cut-rate central core decorated with TPA end-capping groups at 4 and 6-positions. This is the first report of using this dye in PSC devices.

Herein, we have designed and synthesized two innovative and cost effective HTMs, namely, 4,4'-(6,12-bis(octyloxy)-6,12-dihydronaphtho[7,8,1,2,3-*nopqr*]tetraphene-4,10-diyl)bis(*N*,*N*-bis(4-methoxyphenyl)aniline) (TPA-ANT-TPA) and 4,10-bis(1,2-dihydroacenaphthylen-5-yl)-6,12-bis(octyloxy)-6,12-dihydronaphtho[7,8,1,2,3-*nopqr*]tetraphene (ACE-ANT-ACE) using low cost anthanthrone core as starting material (as shown in Scheme 1). Apart from the novelty of using the anthanthrone dye as a precursor, we have used for the first time 1,2-dihydroacenaphthylene (ACE) functional group as an end capping group as well as TPA. TPA-ANT-TPA and ACE-ANT-ACE have been successfully used as HTL in conventional n-i-p perovskite devices. The device structure includes glass/FTO/compact-TiO_2/Mesoporous-TiO_2/$CH_3NH_3PbI_3$/HTL/Ag. First, fluorine doped tin oxide (FTO) commercially available substrates were used as a transparent conducting anode followed by deposition of titanium dioxide (TiO_2) electron transporting compact layer, active perovskite layer and TPA-ANT-TPA & ACE-ANT-ACE based new HTL thin films, respectively. Lastly, silver (Ag) as a cathode electrode was deposited to complete the device fabrication. Further fabrication procedure details can be found in the Supporting Information (ESI†). Under standard illumination (AM 1.5G and 100 mW cm^{-2}), the average PCE of devices using ACE-ANT-ACE and TPA-ANT-TPA HTMs have achieved 11.4% and 16%, respectively. Interestingly, these PCE values are without any additives and they are

comparable to that of doped Spiro-OMeTAD (16.8%) devices under similar working condition. Additionally, after first 20 h in the ambient environment (room temperature, 58% humidity), while the PCE of unsealed Spiro-OMeTAD based devices retained 2% of its initial value, that of TPA-ANT-TPA still retained 80% of its original performance which is one of the most important striking features of our newly developed HTM. After extensive optimization of the metal oxide scaffold and device processing conditions, novel TPA-ANT-TPA HTM based PSCs devices achieved a maximum PCE of 17.5%. The overwhelming advantages such as high performance and higher stability make our newly developed HTMs promising candidates for low cost perovskite solar cell devices.

Novel anthanthrone core derivatives end capped with methoxy triphenylamine at both ends (TPA-ANT-TPA and ACE-ANT-ACE have been designed (**Figure 1**) and synthesized by classical Suzuki coupling. The synthesis is quite straightforward and various steps involved are shown in Scheme 1. Initially, the reaction of 4-bromoaniline (**1**) with 1-iodo-4-methoxybenzene, strong base KOH, CuCl, and 1,10-phenanthroline monohydrate in toluene produced the intermediate 4-bromo-*N*,*N*-bis(4-methoxyphenyl)aniline (**2**). Afterwards, in presence of bis(pinacolato)diboron, strong base potassium acetate, 1, 1'-bis(diphenylphosphino)ferrocene]dichloropalladium(II) catalyst in dimethyl formamide solution, the compound 2 was converted to 4-methoxy-*N*-(4-methoxyphenyl)-*N*-(4-(4,4,5,5-tetramethyl-1,3,2-dioxaborolan-2-yl)phenyl)aniline (**3**) at 120 ^{o}C overnight. Meanwhile, the alkylation of 4,10-dibromoanthanthrone (**4**) at 2 and 6 positions aimed to enhance the solubility and make dibromoanthanthrone become the electron rich unit. The alkylation was operated under base environment of aqueous sodium hydroxide and Aliquat 336, catalyst of sodium dithionite and 1-bromooctane at 80 °C overnight. Then 4,10-dibromo-6,12-bis(octyloxy)anthanthrene (**5)** was collected with high yield. The final HTMs TPA-ANT-TPA and ACE-ANT-ACE were produced based on the Suzuki coupling reaction (2M

potassium carbonate as a base, tetrakis (triphenylphosphine) palladium (0) as catalyst in toluene solvent). ACE-ANT-ACE was synthesized from compound 5 and 2-(1,2-dihydroacenaphthylen-5-yl)-4,4,5,5-tetramethyl-1,3,2-dioxaborolane, whereas TPA-ANT-TPA was made from compound 5 and compound 3. All reactions were stirred at 120 ^{o}C for 48 h. After purification, TPA-ANT-TPA and ACE-ANT-ACE's yield was to be of 60% and 65%. Their purity was proved by proton and C13 nuclear magnetic resonance (NMR) spectroscopy (Figure S1-S5, ESI†). The solubility of these anthanthrone derivatives was extremely good in most common organic solvents such as chloroform, dichloromethane, and chlorobenzene.

To understand the structures and electronic properties of these molecules, density functional theory (DFT) calculations at the B3LYPr level of theory using the basis set 6-31g(d, p) were performed. A PCM model of the chloroform solvent was used.[36] The results are shown in **Figure 1** and summarized in Table S1 (ESI†). The electron density of the LUMO is primarily distributed over the π-conjugated system through the anthanthrone (ANT) core in both molecules. The HOMO of ACE-ANT-ACE has the electron density localized mainly on the ANT unit, whereas for TPA-ANT-TPA, electron density delocalized over the entire molecule including the electron-rich TPA unit as expected. The lack of HOMO density on the ACE moiety is not unusual, as bonded fused aromatic units tend to preserve their HOMO-like orbitals which become HOMO-*n* in the bonded system. HOMO/LUMO energy levels for ACE-ANT-ACE are -4.80/-2.06 eV whereas for TPA-ANT-TPA, is they are -4.67/-2.04 eV respectively. Consequently, the band gap of ACE-ANT-ACE and TPA-ANT-TPA is calculated to be 2.74 and 2.63 eV, respectively. Optical absorption maxima were at 474 nm for ACE-ANT-ACE (HOMO→LUMO dominated) and at 482 nm for TPA-ANT-TPA (dominated by two transitions, HOMO→LUMO at 524 nm and HOMO-2→LUMO at 467 nm), giving optical band gaps of 2.61 and 2.58 eV respectively which are

in a good agreement with the experimentally estimated optical gaps of 2.56 and 2.48 eV (**Table 1**).

The normalized UV-vis absorption (**Figure 2**a) and emission (Figure S6, ESI†) spectra of ACE-ANT-ACE and TPA-ANT-TPA in chloroform (CF) solutions and thin films were measured and the relevant data was listed in Table 1. The pattern of the spectra in the thin films is the same as those of the solutions, which implies that no significant crystallization in thin films.[37] The optical absorption of both materials exhibits strong peaks in the ultraviolet (300 – 350 nm) region and lower ones in the visible (400 – 500 nm) region, which has been noticed in the past attempt regarding small molecular ANT derivatives.[10] Compound ACE-ANT-ACE exhibits the absorption maxima at 461 nm for solution and 467 nm for thin film respectively. The thin film absorbance data of ACE-ANT-ACE is blue-shifted in UV region and slightly red shifted in visible area compared to the solution data. Compound TPA-ANT-TPA unveils absorption maxima at 465 nm for solution and 473 nm for thin film respectively. The absorption spectra of solid-state films illustrate slightly red-shifted and little broadened absorption than those measured in the solution, as is expected due to intermolecular interactions in the solid state. Moreover, the optical absorption spectrum of TPA-ANT-TPA is slightly red-shifted in comparison to ACE-ANT-ACE, which could be ascribed to the higher conjugation and higher electron-donating ability of TPA moiety compared to the 1,2-dihydroacenaphthylene (ACE) moiety. The optical band gap of ACE-ANT-ACE and TPA-ANT-TPA are found to be 2.56 and 2.48 eV, respectively, which was estimated from the onset of solid-state absorption.

As shown in Figure S6 (ESI†), the emission maximum of ACE-ANT-ACE and TPA-ANT-TPA are depicted at 480 and 553 nm, respectively. Stokes shifts were estimated from the gap between the maximum of absorption and emission spectra. These materials possessed a large Stokes shift of 157 and 228 nm compared to that of Spiro-OMeTAD (44 nm)[38]. A

large Stoke shift implies the different and large geometrical changes between the ground- and excited-state geometry and is a reflection of molecular flexibility. This property also enhances the pore filling of a hole transport ability of materials.[38-40]

The thermogravimetric analysis (TGA) was operated under a nitrogen atmosphere in order to investigate the thermal stability of new molecules, which lost less than 5% weight upon heating. The TGA curves were shown in Figure S7 (ESI†) and recorded in Table 1. The decomposition of ACE-ANT-ACE and TPA-ANT-TPA started at temperatures 265 °C and 280 °C, respectively, which shows that the small molecules are thermally stable HTMs for PSCs devices. Upon evaluating these materials in DSC measurement (Figure S8, ESI†), the glass transition temperature (T_g) was not observed but the melting points were measured at 215 °C for ACE-ANT-ACE and 265 °C for TPA-ANT-TPA, respectively. The observed melting temperatures of both compounds are comparable to that of Spiro-OMeTAD (248 ^{o}C).[40]

The experimental estimation of the HOMO and LUMO energy levels of ACE-ANT-ACE and TPA-ANT-TPA were performed using photoelectron spectroscopy in air (PESA) (Figure 2b) and cyclic voltammetry (CV) (Figure S9, ESI†) techniques. The HOMO and LUMO energy level values are presented in the Table 1. In comparison to the HOMO value of active perovskite layer (-5.46 eV), the HOMO value of ACE-ANT-ACE (-5.32 eV) is greater, whereas for TPA-ANT-TPA, the HOMO value (-5.41 eV) is higher than but very close to the perovskite HOMO value. The HOMO values obtained by CV data are also in a good agreement with PESA data. Since the PESA measurements were done in the thin film form they are more relevant to actual devices. As per an earlier report, the hole transport ability can be impended by an excessively small band offset of the HOMO between perovskite and hole injection layers, whereas a very large band offset could cause the reduction of the open-circuit voltage (V_{oc}).[41] Meanwhile, all LUMO values of HTMs are

greater than that of the perovskite layer (-3.93 eV) proving that the new HTMs can block electron transfer to HTL.

After characterizing both new small molecules optically, thermally and electrochemically, the conventional perovskite devices were fabricated with the aim of to study the effect of the hole transport layers on the device performance. PSC devices with the same architecture (FTO/compact-TiO_2/Mesoporous-TiO_2/$CH_3NH_3PbI_3$/HTL/Ag), and different HTM layers were prepared as previously described.[42] The configuration of mesoscopic heterojunction perovskite solar cells was characterized by the cross-sectional scanning electron microscopy (SEM) and shown in Figure 2d. A dense compact-TiO_2 blocking layer (~30 to 40 nm) is first deposited on the FTO substrate by spray pyrolysis, while a mesoporous n-type mp-TiO_2 layer is formed by spin-coating of diluted TiO_2 paste. The $CH_3NH_3PbI_3$ absorber layer was then applied on mesoporous TiO_2 by solvent engineering reported by Seok's group.[43] The perovskite solution was prepared by dissolving 50 wt% of $CH_3NH_3PbI_3$ in the mixed dimethyl sulfoxide (DMSO) and γ- butyrolactone (GBL) DMSO/GBL. Around 120 nm thick HTLs were applied to the top $CH_3NH_3PbI_3$ layer by spin coating. Finally, silver as a counter electrode was deposited by thermal evaporation. The thickness of mesoporous TiO_2 and perovskite is ~550 nm, whereas the capping layer of perovskite is estimated to be ~100 nm. Bigger crystals of TiO_2 in the capping layer assist in saturated light absorption and enhancing the external quantum efficiency (EQE) in the red-light range.

For a valid comparison of performance in terms of PCE and stability, we prepared new dopant-free HTMs based devices and standard devices with dopant using conventional Spiro-OMeTAD (with additional additives, including *t*BP and LiTFSI) as the HTM. The optimized champion device efficiency for three different HTMs and corresponding photovoltaic performance parameters are shown in **Figure 3**a, b and **Table 2**. The TPA-ANT-TPA HTM

based PSC device (Figure 3a) shows the highest champion device efficiency of 17.5% (J_{sc} = 21.07 mA cm^{-2}, V_{oc} = 1.03 V and *FF* = 79.6) whereas a bit lower PCE of 13.1% is recorded with J_{sc} = 18.7 mA cm^{-2}, V_{oc} = 1.03 V and *FF* = 67 in case of ACE-ANT-ACE (Figure 3a). Meanwhile, doped Spiro-OMeTAD-based device performance (Figure 3b) approaches the PCE of 16.8% with J_{sc} of 21.09 mA cm^{-2}, V_{oc} = 1.04 V and *FF* = 76.8. In addition, there is a no hysteresis on the reverse scan (0 V to V_{oc}) at low scan speed of 0.1 V/s for TPA-ANT-TPA and Spiro-OMeTAD based devices. However, for ACE-ANT-ACE HTM based devices, a negligible hysteresis resulted in a lowered PCE from 13.1% to 11%. As per previous discussion, an excessively small band offset of the HOMO between perovskite and HTL may hamper the effective hole transport ability.[41] However, our study significantly showed that even though the work function of TPA-ANT-TPA is very close to that of perovskite active layer, still the better PCE than that of ACE-ANT-ACE could be achieved. The lower V_{oc} of ACE-ANT-ACE is due to the large band offset and HOMO value difference between this compound and active layer perovskite.[41] Furthermore, TPA-ANT-TPA based PSCs shows improvement in short circuit current (J_{sc} = 21.07 mA cm^{-2}) compared to ACE-ANT-ACE (J_{sc} =18.7 mA cm^{-2}) which is due to the shallower HOMO of TPA-ANT-TPA that allows an effective hole extraction.

To the best of our knowledge, the obtained PCE of 17.5% using TPA-ANT-TPA HTM is very high compared to other HTMs reported in the literature taking dopant-free aspect into account.[19, 26, 44, 45] The hysteresis behaviours of champion devices and statistics of a total of 90 devices prepared using three different hole transporting layers is shown in Figure S13, Table 2 and S11 respectively (ESI†). The statistics of total 90 PSCs prepared using TPA-ANT-TPA, ACE-ANT-ACE and Spiro-OMeTAD exhibits an average device efficiency of 16%, 11.4% and 13.8% respectively. As shown in Figure 3c, the devices with TPA-ANT-

297 TPA exhibit EQE values above 78 to 82% from 365 nm to 650 nm covering the entire UV
298 region with the highest EQE of 82% observed at 470 nm.

299 To measure the hole transport properties, a space charge limited current (SCLC)
300 method was used. A spin-coated layer of the HTMs on an ITO/PEDOT-PSS substrate,
301 followed by an evaporated gold counter electrode was prepared for measurements. As the
302 ITO and gold work functions are close to the HTM´s HOMO level, this creates a hole-only
303 device from which the mobility can be determined. The highest hole mobility (Table 2,
304 Figure S14 (ESI†)) of 2.6 x 10^{-4} cm^2 V^{-1} s^{-1} was obtained with TPA-ANT-TPA and was
305 higher than that with Spiro-OMeTAD (1.5 x 10^{-4} cm^2 V^{-1} s^{-1}) and ACE-ANT-ACE (2.4 x 10^{-5}
306 cm^2 V^{-1} s^{-1}). This is consistent with the good fill factor and efficiency performance shown by
307 perovskite devices prepared utilizing TPA-ANT-TPA as HTL.

308 The stability of PSC devices is one of the most critical parameter and most discussed
309 parameter in perovskite solar cell community. Perovskite solar cell stability is also one of the
310 major hurdles to commercialize this technology for the industrial scale. Ambient humidity is
311 one of the most important factors responsible for the quick degradation of PSCs and this is
312 due to the salt type nature of $CH_3NH_3PbI_3$ active layer in PSC.[46-48] We studied the stability
313 of fabricated champion devices without any encapsulation at high humidity conditions
314 (relative humidity (RH) ≥ 58%, temperature = 22^oC, in dark condition) for our newly
315 developed ACE-ANT-ACE, TPA-ANT-TPA and standard classical Spiro-OMeTAD HTMs
316 (as shown in **Figure 4**). A simple stability setup used is shown in Figure S12c, d (ESI†) and
317 photovoltaic performance was measured at 1000 wm^{-2} (AM1.5G) using regular aging
318 intervals. In particular, photovoltaic properties of our novel **TPA-ANT-TPA** and Spiro-
319 OMeTAD in the aging test are detailed in Figure 4a, b. Additionally, the efficiency of all
320 HTMs based devices are evaluated under identical conditions and depicted in Figure 4. The
321 degradation test results show that the Spiro-OMeTAD HTM based devices degraded at a

faster rate compared to **TPA-ANT-TPA** and **ACE-ANT-ACE** HTM based devices. Additionally, we have tested the champion devices using all three HTLs under continuous 1 sun illumination in ambient air for 200 hours exposure (Figure S15, (ESI†)) and found the TPA-ANT-TPA and ACE-ANT-ACE HTM based devices shows a smaller drop in efficiency, and still sustain improved stability over Spiro-OMeTAD based devices.

Moreover, the novel ANT core along with extended TPA groups offers a better surface coverage and in addition the absence of the Li salt also gives better stability[4, 49] for TPA-ANT-TPA and ACE-ANT-ACE HTM based PSCs than that of Spiro-OMeTAD HTL based PSCs. It can be seen that the PCE values diminished rapidly down to ~2% (after only 10 hours) for Spiro-OMeTAD based devices. However, the devices based on TPA-ANT-TPA are seen to be more stable with observed efficiency reduced to ~14% (after >50 hours exposure to 58% RH conditions) and 15% (after 200 hours of continuous illumination to 1 sun in ambient air).

The overall superior performance of PCE and stability of TPA-ANT-TPA over Spiro-OMeTAD provide a promising alternative replacement for high performance perovskite solar cells. The reason for the dramatic improvement in stability of TPA-ANT-TPA based PSCs (compare to Spiro-OMeTAD and ACE-ANT-ACE) and improvement in efficiency from 13% with ACE-ANT-ACE to 17.5% with TPA-ANT-TPA are further investigated by steady state photoluminescence (**Figure 5**a) and morphological measurements (**Figure 6**).

The measurement of steady state photoluminescence based on a simple architecture: Glass/$CH_3NH_3PbI_3$/HTM is shown in Figure 5a. In order to eliminate any quenching effect related to electron transfer to the oxide layer, we avoided to use of a TiO_2 layer while doing PL measurements. During these PL measurements, we have to make sure that the photoluminescence quenching is only caused by the hole transport layer and is not due to any other materials. All the HTL thin films were excited at 550 nm wavelength. From the data, it

is quite clear that the bare perovskite film without any HTM (black curve) exhibits a high PL emission intensity as a result of the formation of good quality (crystallinity and homogeneous surface) perovskite film. Such observations are similar to our earlier studies and they are also comparable with reported data.[42, 50] Upon deposition of HTM on the perovskite layer, a significant reduction in PL emission was observed. Perovskite films covered with TPA-ANT-TPA (blue curve) and ACE-ANT-ACE (green curve) HTL's display a stronger PL quenching (~95 to 80%) than the films covered with Spiro-OMeTAD (~60 to 65%) HTL. These results clearly indicate a higher PL quenching ability of our newly developed TPA-ANT-TPA and ACE-ANT-ACE materials compared to Spiro-OMeTAD. Between the two materials, TPA-ANT-TPA exhibits more efficient exciton dissociation efficiency and ensures a more efficient charge generation and high hole mobility as well as low recombination at the TPA-ANT-TPA/$CH_3NH_3PbI_3$ interface.

The time resolved photoluminescence measurement was performed and shown in Figure 5b to verify the improved hole transport properties. Bare perovskite films deposited on glass substrate as well as with different hole transport layers show biphasic kinetics. The fast component decays in picosecond (due to 80 ps laser pulse) and the slower component has a time constant of 10-15 ns. The fast component represents trap filling. As the hole transfer films are deposited on bare glass - perovskite layer for direct probing, this gives us a good estimation about quenching of the photoluminescence due to hole transport layers. As shown in our previous work, a good quality glass-perovskite sample shows a lifetime of 8-10 ns.[50] In this case, similarly we have obtained 8 ns lifetime for the bare perovskite sample (without the hole transporting layer). This, along with the high intensity PL, further confirms the quality of the perovskite film. Bare perovskite films show an average life time of 200 ns. After the introduction of TPA-ANT-TPA hole transporting layer above the perovskite layer the average decay time (τ) shortened to ~20.2 ns. The fast decay lifetime (τ_1) of all 3 hole

transporting materials decreased from 33 ns (bare perovskite without HTL) to 20 ns for ACE-ANT-ACE, to 12 ns for Spiro-OMeTAD and 6 ns for TPA-ANT-TPA hole transporting layer. At the same time the weight fraction increased from 3% (bare perovskite film) to 15% for ACE-ANT-ACE hole transport layer, 27.2% for Spiro-OMeTAD and 32.5% for TPA-ANT-TPA hole transport layers. This clearly shows improved hole extraction as well charge dissociation from perovskite to deposited hole transport layers. The order of effective hole extraction follows a trend: TPA-ANT-TPA > Spiro-OMeTAD > ACE-ANT-ACE.

Figure 6 exhibits scanning electron microscope (SEM) images recoded on the perovskite thin film deposited on top of FTO/compact TiO_2/mesoporous TiO_2 substrates, TPA-ANT-TPA and ACE-ANT-ACE on perovskite layer, respectively. Figure 6a clearly shows the perovskite film with a high coverage and a crystal size ranging from 100 to 300 nm. Figure 6b, c, and d1 illustrate similar surface thicknesses of TPA-ANT-TPA, Spiro-OMeTAD, and ACE-ANT-ACE HTM layers under the same magnification. Among all of the data, Figure 6b obviously shows uniform, defect-free coverage of TPA-ANT-TPA HTM. For Spiro-OMeTAD HTM, weak hydrogen bonding between active $CH_3NH_3PbI_3$ layer and HTM might be responsible factor for poor morphology than TPA-ANT-TPA. Interface between HTM and $CH_3NH_3PbI_3$ helps in stabilization of the perovskite phase with a uniform and dense morphology as well as improved crystallites. Such arrangement is responsible for the highly-improved cell performance. Relatively less homogeneous surface is seen for ACE-ANT-ACE HTL whereas for Spiro-OMeTAD, the surface is more inhomogeneous with a rough surface morphology (Figure 6d) and at some point, showing crystallization possibly caused by the use of dopants (Figure 6d1). Spin coated Spiro-OMeTAD HTL shows oriented aggregation or crystallization due to its intrinsic features.[51] Also, spin coated films of ACE-ANT-ACE and TPA-ANT-TPA films shows small particles which could be attributed with aggregation.

These electron microscope observations strongly correlate with the perovskite solar cell stability trends observed in Figure 4. The improved coverage of the TPA-ANT-TPA films resulted in devices with much higher stability whereas the HTM films with small to large pin-holes exhibited lower stability. The good coverage of the HTM on the perovskite layer is an extremely important parameter besides its hole transporting ability. It assures protection of the perovskite thin film layer from the exposure to oxygen,[47] humidity,[48, 52] and heat.[52] These external exposures are main culprits for the quick degradation of PSCs under ambient conditions. In addition to the surface morphology of HTMs on perovskite layer, we also performed contact angle measurements (Figure S10, ESI†) on TPA-ANT-TPA and ACE-ANT-ACE deposited thin films on perovskite layer to confirm the hydrophobicity of the surface. The obtained data show a bad wetting behaviour with an elevated angle (85^{o}) of water droplets for TPA-ANT-TPA surface, whereas a good wetting was observed with a lower contact angle (47^{o}) for the Spiro-OMeTAD layer. The higher stability of TPA-ANT-TPA based PSCs is due to its higher hydrophobic nature that will protect the perovskite layer underneath. To further investigate the stability of all three HTMs, TPA-ANT-TPA, ACE-ANT-ACE and Spiro-OMeTAD are deposited on the perovskite layer and are subjected to 1 sun (AM 1.5G) continuous illumination for two weeks.

The crystalline and absorbing characteristics of the perovskite covered with the three different HTLs before and after 1 sun illumination for 2 weeks are measured using XRD and UV-visible spectroscopy as shown in Figure S16, ESI†. The perovskite covered with TPA-ANT-TPA and ACE-ANT-ACE does not show any sign of degradation and perovskite layers underneath continue to show high crystallinity and absorbance after 2 weeks of continuous 1 sun illumination (Figure S16(a), (b), (c), (d), ESI†). However, the perovskite layer covered with Spiro-OMeTAD shows complete degradation of the perovskite to PbI_2 as observed from Figure S16(c), (f), ESI†.

A comparison of lab cost difference between TPA-ANT-TPA and Spiro-OMeTAD HTMs is given in Table 3. The synthesis cost of TPA-ANT-TPA is estimated by using the price of chemical suppliers in Australia and following previous attempts.[53, 54] Its further details can be found in Table S2-5 (ESI†). The flowchart describing the synthesis of 1g of TPA-ANT-TPA was illustrated in Figure S17 (ESI†). Meanwhile, the price of synthetic Spiro-OMeTAD's HTM is surveyed from earlier reports and its commercial price is also mentioned.[53, 55] The cost of our newly developed high performance TPA-ANT-TPA HTM (taking both efficiency and stability into an account) is roughly two third that of synthetic Spiro-OMeTAD and it can further drop if large scale synthesis is performed.

A brief comparison among dopant-free HTMs using TPA moiety as either the central core or the end-capping groups has been conducted and listed in **Table 4**. These preferred HTMs have similar device structure: FTO/compactTiO_2/mesoporous TiO_2/$CH_3NH_3PbI_3$/HTM/cathode with approximately equivalent working area. Their photovoltaic parameters of the solar cells were evaluated under 1 sunlight illumination (100 mW cm^{-2}) condition. Overall, the device with TPA-ANT-TPA as HTM displays the highest FF whereas the V_{oc} and J_{sc} are among the best values in comparison with other ones. This material also possesses the impressive hole mobility which may be a trigger to the superior values of the FF and J_{sc}. Even though the TPA-CN and TPA-ANT-TPA based devices exhibited the similar efficiency (17.5%), the performance of TPA-CN was lower than that of the reference device based on Spiro-OMeTAD under similar conditions.[35] During the ageing test without encapsulation at room temperature, the PCE achieved using our TPA-ANT-TPA as HTM maintained 80% of the initial value. Even thought this may be lower than that of Z34, Me-QTPA, EDOT-OMeTPA, and Z1011, their initial performance was worse than that of our material based devices. According to the tabular comparison, our novel TPA-ANT-TPA HTM can become a suitable and promising alternative to Spiro-OMeTAD.

Overall, the better performance and stability properties of PSCs made using TPA-ANT-TPA based hole transport layers are due to the following factors: (a) better charge extraction - the experimental photoluminescence spectroscopy shows enhanced quenching for TPA-ANT-TPA based perovskite devices due to better hole transfer. Additionally, it is also a result of close alignment of HOMO energy levels of the HTM and perovskite with minimal band offset; (b) stability improvement - the improved morphology, uniformity and a good surface coverage of the capping layer of TPA-ANT-TPA. The hydrophobic nature of the TPA-ANT-TPA surface as seen from contact angle measurements makes the PSCs made from TPA-ANT-TPA HTM more stable than Spiro-OMeTAD based devices. Moreover, avoiding the use of dopants such as LiTFSI enhances the stability (salts often reacts quickly with moisture).

In this work, we have successfully designed and synthesized two new small molecular TPA-ANT-TPA and ACE-ANT-ACE HTMs based on an innovative anthanthrone dye as a core. The syntheses of both materials were conducted via a simple coupling protocol using a common anthanthrone dye as a central core and two different tri-phenylamine and acenaphthylene end-capping units. A detailed comparison on optoelectronic properties of TPA-ANT-TPA and ACE-ANT-ACE based PSCs has been performed and it is found that a HOMO energy level of TPA-ANT-TPA is close to the active perovskite energy level for better hole transport with minimal energy offset. Upon evaluating both TPA-ANT-TPA and ACE-ANT-ACE as hole transporting materials in perovskite solar cell devices, the highest power conversion efficiency of 13% and 17.5% has been achieved, respectively. The TPA-ANT-TPA HTM not only exhibits high performance showing champion efficiency of 17.5% and average efficiency of 16% with increased reproducibility of PSCs as compared to Spiro-OMeTAD based PSCs but also shows a lower cost and straightforward synthesis with easy purification. One of the most important striking features of TPA-ANT-TPA based PSC

devices is its environmental stability which is much higher than that with classical Spiro-OMeTAD. This is a most critical parameter, and the most discussed aspects in the perovskite solar cell community. The significantly higher stability of the TPA-ANT-TPA based devices is due to the hydrophobic nature and homogeneous coverage as a result of more extended chemical structure of TPA on the perovskite capping layer. The TPA-ANT-TPA HTM without additives resulted in increased V_{oc} and improved moisture resistance of PSCs, as a result of more uniform formation of TPA-ANT-TPA capping layer on the surface of perovskite leading to a more efficient hole transport than with Spiro-OMeTAD. The improved charge collection efficiency in devices prepared with TPA-ANT-TPA HTL (as seen from effective PL quenching) compared to that of ACE-ANT-ACE and Spiro-OMeTAD HTL leads to higher short circuit current and photovoltage. In summary, we successfully demonstrated the great potential of a low cost anthanthrone dye as a starting precursor for designing highly efficient HTMs for stable and low cost efficient PSCs. Using such efficient, stable and low cost HTMs, it must be possible to produce the large-scale roll-to-roll printed perovskite solar cell modules and prototypes for commercialization and energy harvesting application.

Experimental Section

Detailed experimental methods can be found in the Supporting Information.

Supporting Information

Supporting Information is available from the Wiley Online Library or from the author.

Acknowledgement

H.D.P is thankful to QUT for offering here QUTPRA scholarship to conduct his research work. Some of the data reported in this paper were obtained at the Central Analytical Research Facility operated by the Institute for Future Environments (QUT). Access to CARF is supported by generous funding from the Science and Engineering Faculty (QUT). Author S. M. J. is thankful to Welsh assembly Government funded Sêr Cymru Solar project, EPSRC grants EP/M025020/1 (Supergen Solar Challenge) and Marie-Curie COFUND fellowship for financial support. S.M. is supported by the Ministry of Education of Singapore. Additionally, this project has received funding from the European Union's Horizon 2020 research and innovation programme under the Marie Skłodowska-Curie grant agreement No 663830. P.S. is thankful to QUT for the financial support from the Australian Research Council (ARC) for the Future Fellowship (FT130101337) and QUT core funding (QUT/ 322120-0301/07).

References

[1] a) C. Battaglia, A. Cuevas, S. De Wolf, *Energy Environ. Sci.* **2016**, *9*, 1552; b) S. De Wolf, A. Descoeudres, Z. C. Holman, C. Ballif, *Green* **2012**, *2*, 7.

[2] a) J. Gong, K. Sumathy, Q. Qiao, Z. Zhou, *Renew. Sustainable Energy Rev.* **2017**, *68*, 234; b) M. Pazoki, U. B. Cappel, E. M. J. Johansson, A. Hagfeldt, G. Boschloo, *Energy Environ. Sci.* **2017**, *10*, 672.

[3] a) P. Cheng, X. Zhan, *Chem. Soc. Rev.* **2016**, *45*, 2544; b) Q. An, F. Zhang, J. Zhang, W. Tang, Z. Deng, B. Hu, *Energy Environ. Sci.* **2016**, *9*, 281.

[4] T. A. Berhe, W.-N. Su, C.-H. Chen, C.-J. Pan, J.-H. Cheng, H.-M. Chen, M.-C. Tsai, L.-Y. Chen, A. A. Dubale, B.-J. Hwang, *Energy Environ. Sci.* **2016**, *9*, 323.

[5] S. Yang, W. Fu, Z. Zhang, H. Chen, C.-Z. Li, *J. Mater. Chem. A* **2017**, *5* 11462.

[6] G. Hodes, *Science* **2013**, *342*, 317.

[7] a) P.-Y. Chang, P.-H. Wang, W.-C. Lin, C.-H. Yang, *New J. Chem.* **2016**, *40*, 9725; b) M. Liang, J. Chen, *Chem. Soc. Rev.* **2013**, *42*, 3453; c) W. Zeng, Y. Cao, Y. Bai, Y. Wang, Y. Shi, M. Zhang, F. Wang, C. Pan, P. Wang, *Chem. Mater.* **2010**, *22*, 1915; d) K. S. V. Gupta, T. Suresh, S. P. Singh, A. Islam, L. Han, M. Chandrasekharam, *Org. Electron.* **2014**, *15*, 266.

[8] a) P. Sonar, G.-M. Ng, T. T. Lin, A. Dodabalapur, Z.-K. Chen, *J. Mater. Chem.* **2010**, *20*, 3626; b) A. Tang, C. Zhan, J. Yao, E. Zhou, *Adv. Mater.* **2017**, *29*, 1600013; c) Y. Li, P. Sonar, L. Murphy, W. Hong, *Energy Environ. Sci.* **2013**, *6*, 1684; d) R. Stalder, J. Mei, K. R. Graham, L. A. Estrada, J. R. Reynolds, *Chem. Mater.* **2014**, *26*, 664.

[9] a) M. S. Kang, S. D. Sung, I. T. Choi, H. Kim, M. Hong, J. Kim, W. I. Lee, H. K. Kim, *ACS Appl. Mater. Interfaces* **2015**, *7*, 22213; b) B. Xu, E. Sheibani, P. Liu, J. Zhang, H. Tian, N. Vlachopoulos, G. Boschloo, L. Kloo, A. Hagfeldt, L. Sun, *Adv. Mater.* **2014**, *26*, 6629; c) W. Li, M. Otsuka, T. Kato, Y. Wang, T. Mori, T. Michinobu, *Beilstein J. Org. Chem.* **2016**, *12*, 1401.

[10] Y. Geng, C. Yi, M. P. Bircher, S. Decurtins, M. Cascella, M. Grätzel, S.-X. Liu, *RSC Adv.* **2015**, *5*, 98643.

[11] a) J.-B. Giguère, N. S. Sariciftci, J.-F. Morin, *J. Mater. Chem. C* **2015**, *3*, 601; b) B. K. Shah, D. C. Neckers, J. Shi, E. W. Forsythe, D. Morton, *J. Phys. Chem. A* **2005**, *109*, 7677.

[12] Y. J. Kim, J. S. Lee, J. Hong, Y. Kim, S. B. Lee, S.-K. Kwon, Y.-H. Kim, C. E. Park, *J. Polym. Sci. A Polym. Chem.* **2016**, *54*, 2559.

[13] J. B. Giguere, Q. Verolet, J. F. Morin, *Chemistry* **2013**, *19*, 372.

[14] A. Lafleur-Lambert, J.-B. Giguère, J.-F. Morin, *Polym. Chem.* **2015**, *6*, 4859.

[15] J. B. Giguere, J. Boismenu-Lavoie, J. F. Morin, *J. Org. Chem.* **2014**, *79*, 2404.

[16] A. Lafleur-Lambert, J.-B. Giguère, J.-F. Morin, *Macromolecules* **2015**, *48*, 8376.

[17] A. Kojima, K. Teshima, Y. Shirai, T. Miyasaka, *J. Am. Chem. Soc.* **2009**, *131*, 6050.

[18] a) Best research-cell efficiencies, https://www.nrel.gov/pv/assets/images/efficiency-chart.png (accessed: October 2017); b) W. S. Yang, B.-W. Park, E. H. Jung, N. J. Jeon, Y. C. Kim, D. U. Lee, S. S. Shin, J. Seo, E. K. Kim, J. H. Noh, S. I. Seok, *Science* **2017**, *356*, 1376.

[19] Y.-K. Wang, Z.-C. Yuan, G.-Z. Shi, Y.-X. Li, Q. Li, F. Hui, B.-Q. Sun, Z.-Q. Jiang, L.-S. Liao, *Adv. Funct. Mater.* **2016**, *26*, 1375.

[20] N. H. Tiep, Z. Ku, H. J. Fan, *Adv. Energy Mater.* **2016**, *6*, 1501420.

[21] D. Bi, W. Tress, M. I. Dar, P. Gao, J. Luo, C. Renevier, K. Schenk, A. Abate, F. Giordano, J.-P. C. Baena, J.-D. Decoppet, S. M. Zakeeruddin, M. K. Nazeeruddin, M. Grätzel, A. Hagfeldt, *Sci. Adv.* **2016**, *2*, e1501170.

[22] M. Saliba, S. Orlandi, T. Matsui, S. Aghazada, M. Cavazzini, J.-P. Correa-Baena, P. Gao, R. Scopelliti, E. Mosconi, K.-H. Dahmen, F. De Angelis, A. Abate, A. Hagfeldt, G. Pozzi, M. Graetzel, M. K. Nazeeruddin, *Nat. Energy* **2016**, *1*, 15017.

[23] a) F. Zhang, W. Shi, J. Luo, N. Pellet, C. Yi, X. Li, X. Zhao, T. J. S. Dennis, X. Li, S. Wang, Y. Xiao, S. M. Zakeeruddin, D. Bi, M. Gratzel, *Adv. Mater.* **2017**, *29*, 1606806; b) D. Bi, C. Yi, J. Luo, J.-D. Décoppet, F. Zhang, Shaik M. Zakeeruddin, X. Li, A. Hagfeldt, M. Grätzel, *Nat. Energy* **2016**, *1*, 16142.

[24] a) H. Wei, J. Xiao, Y. Yang, S. Lv, J. Shi, X. Xu, J. Dong, Y. Luo, D. Li, Q. Meng, *Carbon* **2015**, *93*, 861; b) I. Lim, E.-K. Kim, S. A. Patil, D. Y. Ahn, W. Lee, N. K. Shrestha, J. K. Lee, W. K. Seok, C.-G. Cho, S.-H. Han, *RSC Adv.* **2015**, *5*, 55321.

[25] a) H. Zhang, H. Wang, W. Chen, A. K. Jen, *Adv. Mater.* **2017**, *29*, 1604984; b) J. W. Jung, C. C. Chueh, A. K. Jen, *Adv. Mater.* **2015**, *27*, 7874.

[26] J. Liu, Y. Wu, C. Qin, X. Yang, T. Yasuda, A. Islam, K. Zhang, W. Peng, W. Chen, L. Han, *Energy Environ. Sci.* **2014**, *7*, 2963.

[27] B. Xu, D. Bi, Y. Hua, P. Liu, M. Cheng, M. Grätzel, L. Kloo, A. Hagfeldt, L. Sun, *Energy Environ. Sci.* **2016**, *9*, 873.

[28] a) G.-W. Kim, G. Kang, J. Kim, G.-Y. Lee, H. I. Kim, L. Pyeon, J. Lee, T. Park, *Energy Environ. Sci.* **2016**, *9*, 2326; b) Y. S. Kwon, J. Lim, H.-J. Yun, Y.-H. Kim, T. Park, *Energy Environ. Sci.* **2014**, *7*, 1454.

[29] a) J. Wang, K. Liu, L. Ma, X. Zhan, *Chem. Rev.* **2016**, *116*, 14675; b) S. S. Reddy, K. Gunasekar, J. H. Heo, S. H. Im, C. S. Kim, D. H. Kim, J. H. Moon, J. Y. Lee, M. Song, S. H. Jin, *Adv. Mater.* **2016**, *28*, 686; c) Z. Yu, L. Sun, *Adv. Energy Mater.* **2015**, *5*, 1500213.

[30] Y. Yue, N. Salim, Y. Wu, X. Yang, A. Islam, W. Chen, J. Liu, E. Bi, F. Xie, M. Cai, L. Han, *Adv. Mater.* **2016**, *28*, 10738.

[31] a) Y. Li, Z. Xu, S. Zhao, B. Qiao, D. Huang, L. Zhao, J. Zhao, P. Wang, Y. Zhu, X. Li, X. Liu, X. Xu, *Small* **2016**, *12*, 4902; b) S. Park, J. H. Heo, C. H. Cheon, H. Kim, S. H. Im, H. J. Son, *J. Mater. Chem. A* **2015**, *3*, 24215; c) K. Rakstys, A. Abate, M. I. Dar, P. Gao, V. Jankauskas, G. Jacopin, E. Kamarauskas, S. Kazim, S. Ahmad, M. Gratzel, M. K. Nazeeruddin, *J. Am. Chem. Soc.* **2015**, *137*, 16172; d) X. Liu, X. Zheng, Y. Wang, Z. Chen, F. Yao, Q. Zhang, G. Fang, Z. K. Chen, W. Huang, Z. X. Xu, *ChemSusChem.* **2017**, *10*, 2833.

[32] a) F. Zhang, C. Yi, P. Wei, X. Bi, J. Luo, G. Jacopin, S. Wang, X. Li, Y. Xiao, S. M. Zakeeruddin, M. Grätzel, *Adv. Energy Mater.* **2016**, *6*, 1600401; b) A. Krishna and A. Grimsdale, *J. Mater. Chem. A*, **2017**, 5, 16446; c) Z. H. Bakr, Q. Wali, A. Fakharuddin, L. Schmidt-Mendec, T. M. Brown, R. Jose, *Nano Energy* **2017**, *34*, 271.

[33] F. Zhang, X. Liu, C. Yi, D. Bi, J. Luo, S. Wang, X. Li, Y. Xiao, S. M. Zakeeruddin, M. Gratzel, *ChemSusChem.* **2016**, *9*, 2578.

[34] F. Zhang, X. Zhao, C. Yi, D. Bi, X. Bi, P. Wei, X. Liu, S. Wang, X. Li, S. M. Zakeeruddin, M. Grätzel, *Dyes Pigm.* **2017**, *136*, 273.

[35] S. Paek, P. Qin, Y. Lee, K. T. Cho, P. Gao, G. Grancini, E. Oveisi, P. Gratia, K. Rakstys, S. A. Al-Muhtaseb, C. Ludwig, J. Ko, M. K. Nazeeruddin, *Adv. Mater.* **2017**, *29*.

[36] a) A. D. Becke, *J. Chem. Phys.* **1993**, *98*, 5648; b) P. Hohenberg, W. Kohn, *Phys. Rev.* **1964**, *136*, B864; c) W. Kohn, L. Sham, *Phys. Rev.* **1965**, *140*, A1133.

[37] J. Wang, S. Wang, X. Li, L. Zhu, Q. Meng, Y. Xiao, D. Li, *Chem. Commun.* **2014**, *50*, 5829.

[38] W. J. Chi, P. P. Sun, Z. S. Li, *Nanoscale* **2016**, *8*, 17752.

[39] D. Alberga, G. F. Mangiatordi, F. Labat, I. Ciofini, O. Nicolotti, G. Lattanzi, C. Adamo, *J. Phys. Chem. C* **2015**, *119*, 23890.

[40] H. Li, K. Fu, A. Hagfeldt, M. Gratzel, S. G. Mhaisalkar, A. C. Grimsdale, *Angew. Chem. Int. Ed. Engl.* **2014**, *53*, 4085.

[41] W.-J. Yin, J.-H. Yang, J. Kang, Y. Yan, S.-H. Wei, *J. Mater. Chem. A* **2015**, *3*, 8926.

[42] S. M. Jain, B. Philippe, E. M. J. Johansson, B.-w. Park, H. Rensmo, T. Edvinsson, G. Boschloo, *J. Mater. Chem. A* **2016**, *4*, 2630.

[43] N. J. Jeon, J. H. Noh, Y. C. Kim, W. S. Yang, S. Ryu, S. I. Seok, *Nat. Mater.* **2014**, *13*, 897.

[44] S. Kazim, F. J. Ramos, P. Gao, M. K. Nazeeruddin, M. Grätzel, S. Ahmad, *Energy Environ. Sci.* **2015**, *8*, 1816.

[45] M. Franckevičius, A. Mishra, F. Kreuzer, J. Luo, S. M. Zakeeruddin, M. Grätzel, *Mater. Horiz.* **2015**, *2*, 613.

[46] Y. Hou, H. Zhang, W. Chen, S. Chen, C. O. R. Quiroz, H. Azimi, A. Osvet, G. J. Matt, E. Zeira, J. Seuring, N. Kausch-Busies, W. Lövenich, C. J. Brabec, *Adv. Energy Mater.* **2015**, *5*, 1500543.

[47] J. Yang, B. D.Siempelkamp, D. Liu, L. K. Timothy, *ACS Nano* **2015**, *9*, 1955.

[48] J. S. Manser, M. I. Saidaminov, J. A. Christians, O. M. Bakr, P. V. Kamat, *Acc. Chem. Res.* **2016**, *49*, 330.

[49] a) Y. Rong, L. Liu, A. Mei, X. Li, H. Han, *Adv. Energy Mater.* **2015**, *5*, 1501066; b) T. Leijtens, G. E. Eperon, N. K. Noel, S. N. Habisreutinger, A. Petrozza, H. J. Snaith, *Adv. Energy Mater.* **2015**, *5*, 1500963.

[50] S. M. Jain, Z. Qiu, L. Häggman, M. Mirmohades, M. B. Johansson, T. Edvinsson, G. Boschloo, *Energy Environ. Sci.* **2016**, *9*, 3770.

[51] a) B. Xu, J. Zhang, Y. Hua, P. Liu, L. Wang, C. Ruan, Y. Li, G. Boschloo, E. M. J. Johansson, L. Kloo, A. Hagfeldt, A. K. Y. Jen, L. Sun, *Chem* **2017**, *2*, 676; b) C. Lu, I. T. Choi, J. Kim, H. K. Kim, *J. Mater. Chem. A* **2017**, *5*, 20263.

[52] W. H. Nguyen, C. D. Bailie, E. L. Unger, M. D. McGehee, *J. Am. Chem. Soc.* **2014**, *136*, 10996.

[53] M. L. Petrus, T. Bein, T. J. Dingemans, P. Docampo, *J. Mater. Chem. A* **2015**, *3*, 12159.

[54] T. P. Osedach, T. L. Andrew, V. Bulović, *Energy Environ. Sci.* **2013**, *6*, 711.

631 [55] a) T. Malinauskas, M. Saliba, T. Matsui, M. Daskeviciene, S. Urnikaite, P. Gratia, R.
632 Send, H. Wonneberger, I. Bruder, M. Graetzel, V. Getautis, M. K. Nazeeruddin, *Energy*
633 *Environ. Sci.* **2016**, *9*, 1681; b) X. Liu, F. Kong, T. Cheng, W. Chen, Z. Tan, T. Yu, F. Guo,
634 J. Chen, J. Yao, S. Dai, *ChemSusChem.* **2017**, *10*, 968.

635 [56] X. Liu, L. Zhu, F. Zhang, J. You, Y. Xiao, D. Li, S. Wang, Q. Meng, X. Li, *Energy*
636 *Technol.* **2017**, *5*, 312.

637 [57] X. Liu, F. Zhang, X. Liu, M. Sun, S. Wang, D. Li, Q. Meng, X. Li, *J. Energy Chem.*
638 **2016**, *25*, 702.

639 [58] L. Cabau, I. Garcia-Benito, A. Molina-Ontoria, N. F. Montcada, N. Martin, A. Vidal-
640 Ferran, E. Palomares, *Chem. Commun.* **2015**, *51*, 13980.

641 [59] H. Choi, S. Paek, N. Lim, Y. H. Lee, M. K. Nazeeruddin, J. Ko, *Chem. Eur. J.* **2014**,
642 *20*, 10894.

643 [60] S. Lv, L. Han, J. Xiao, L. Zhu, J. Shi, H. Wei, Y. Xu, J. Dong, X. Xu, D. Li, S. Wang,
644 Y. Luo, Q. Meng, X. Li, *Chem. Commun.* **2014**, *50*, 6931.

645 [61] L. Zhu, J. Xiao, J. Shi, J. Wang, S. Lv, Y. Xu, Y. Luo, Y. Xiao, S. Wang, Q. Meng,
646 X. Li, D. Li, *Nano Res.* **2014**, *8*, 1116.

647 [62] M. Sun, X. Liu, F. Zhang, H. Liu, X. Liu, S. Wang, Y. Xiao, D. Li, Q. Meng, X. Li,
648 *Appl. Surf. Sci.* **2017**, *416*, 124.

649 [63] S. Lv, Y. Song, J. Xiao, L. Zhu, J. Shi, H. Wei, Y. Xu, J. Dong, X. Xu, S. Wang, Y.
650 Xiao, Y. Luo, D. Li, X. Li, Q. Meng, *Electrochim. Acta* **2015**, *182*, 733.

651 [64] X. Zhao, F. Zhang, C. Yi, D. Bi, X. Bi, P. Wei, J. Luo, X. Liu, S. Wang, X. Li, S. M.
652 Zakeeruddin, M. Grätzel, *J. Mater. Chem. A* **2016**, *4*, 16330.

653 [65] P. Qi, F. Zhang, X. Zhao, X. Liu, X. Bi, P. Wei, Y. Xiao, X. Li, S. Wang, *Energy*
654 *Technol.* **2017**, *5*, 1173.

655 [66] Y. Song, S. Lv, X. Liu, X. Li, S. Wang, H. Wei, D. Li, Y. Xiao, Q. Meng, *Chem.*
656 *Commun.* **2014**, *50*, 15239.

657

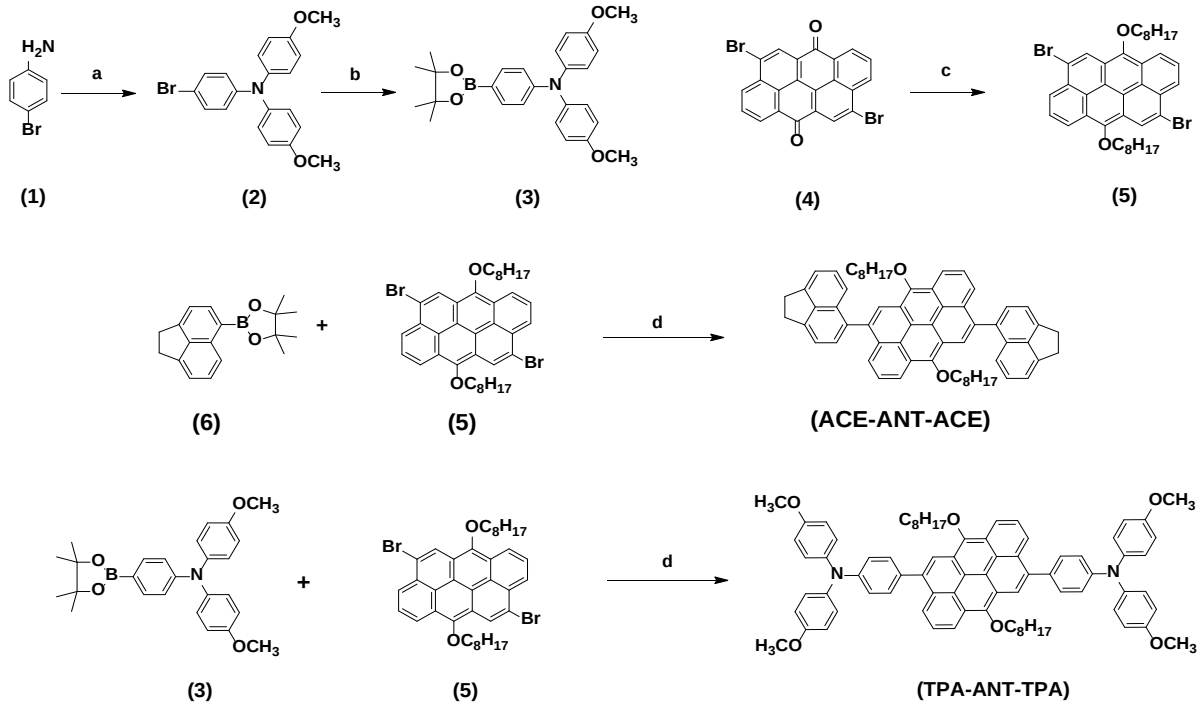

Scheme 1. Synthetic approach to ACE-ANT-ACE and TPA-ANT-TPA. Reagent and conditions: (a) 1-iodo-4-methoxybenzene, KOH, CuCl, 1,10-phenanthroline monohydrate, toluene, 120 ^{o}C, overnight; (b) bis(pinacolato)diboron, KOAc, Pd(dppf)Cl_2, DMF, 120 ^{o}C, overnight; (c) $Na_2S_2O_4$, $C_8H_{17}Br$, aliquat 336, NaOH (aq.), 120 ^{o}C, overnight; (d) 2M K_2CO_3, toluene, $Pd(PPh_3)_4$, 120 ^{o}C,48 h.

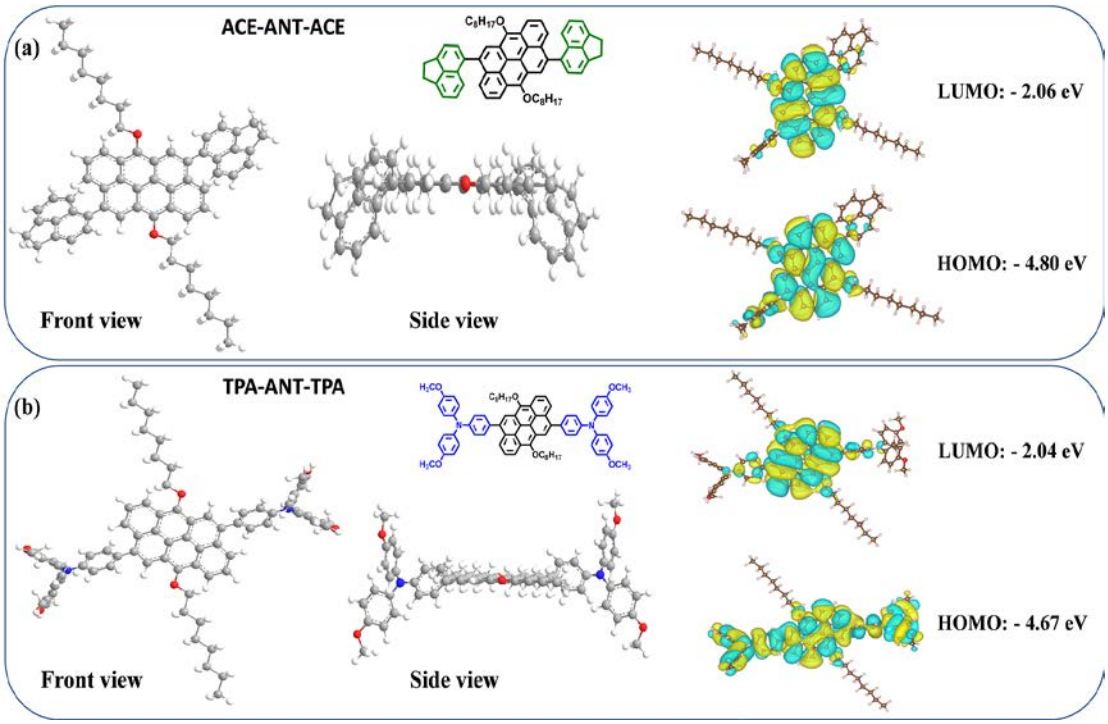

664

665 **Figure 1.** Chemical structures, geometrical configuration (front view and side view), and
666 calculated isosurfaces and energy levels of HOMO and LUMO orbital surfaces of (a) ACE-
667 ANT-ACE and (b) TPA-ANT-TPA.

668

669

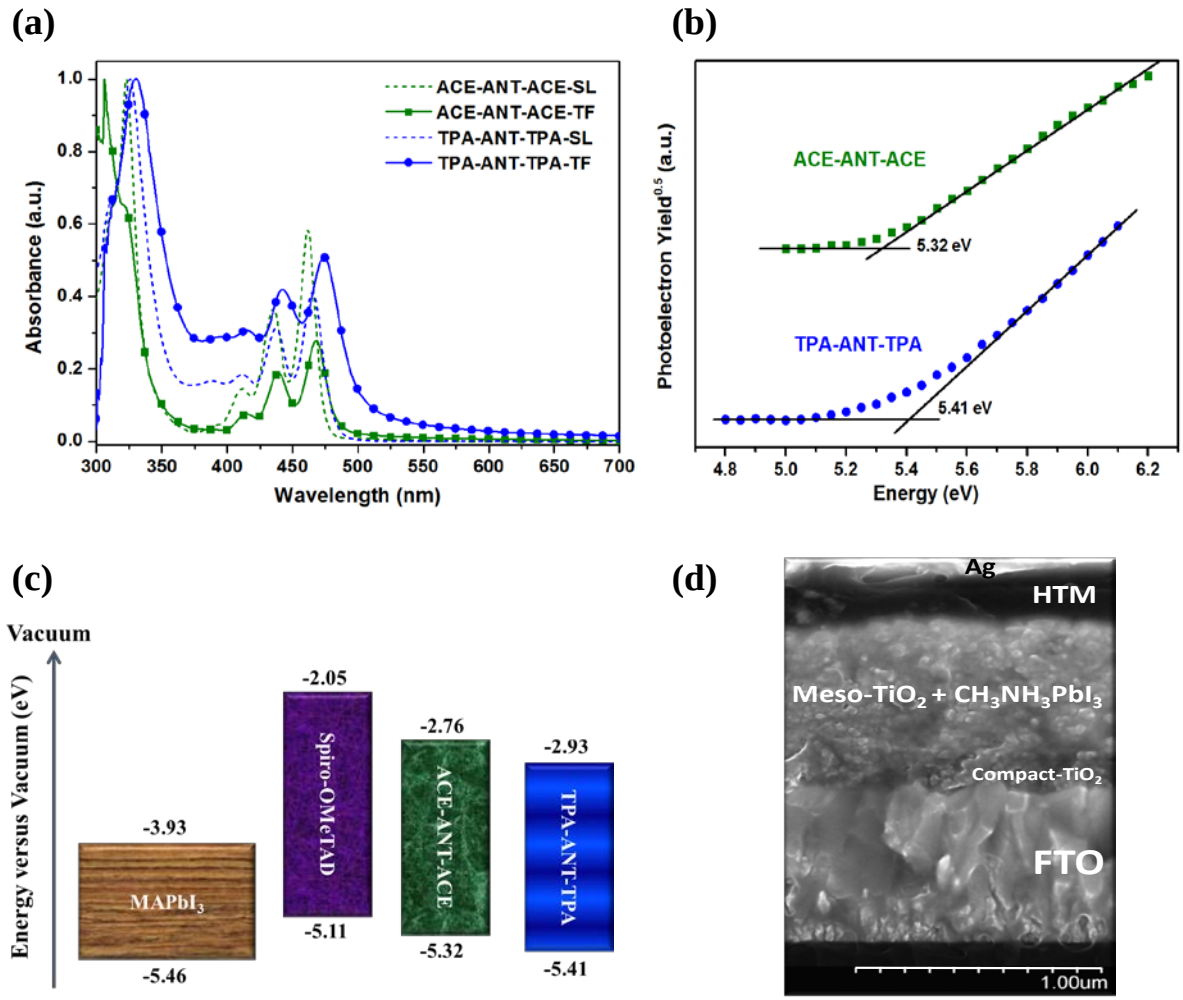

Figure 2. (a) UV-Vis absorption spectra in CF solutions (dash line) and films (solid line), (b) Photoelectron spectroscopy in air (PESA) spectra, (c) Energy level diagrams, (d) Cross-sectional scanning electron microscopy image of PSC without dopants.

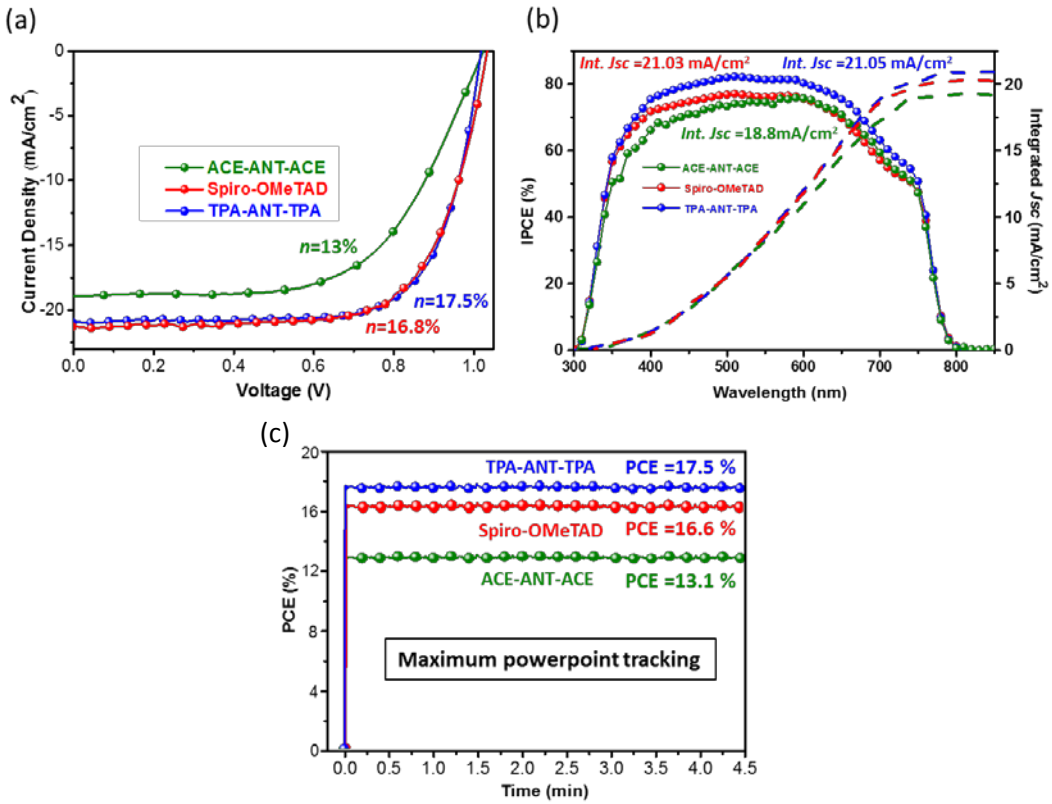

676

677 **Figure 3.** Photovoltaic performance with hysteresis of optimized champion PSC devices
678 made using different hole transport layers: (a) Using ACE-ANT-ACE (green curve) TPA-
679 ANT-TPA (blue curve) as the hole transporting layer and Spiro- OMeTAD (red curve and
680 black curve) as the hole transporting layer; and (b) Absolute EQE spectra (solid line) and
681 integrated current densities (dashed lines) of optimized PSC solar cells prepared using
682 different hole transporting layers as ACE-ANT-ACE (green), TPA-ANT-TPA (blue) and
683 Spiro-OMeTAD (red). (c) Power output under maximum power point tracking for 270 s,
684 starting from forward bias and resulting in a stabilized power output of 17.5%, 16.6% and
685 13% for TPA-ANT-TPA, ACE-ANT-ACE and Spiro-OMeTAD based devices respectively
686 (at 960 mV). The voltage scan rate for all scans was 10 mVs^{-1} and no device preconditioning,
687 such as light soaking or forward voltage bias applied for a long time, was applied before
688 starting the measurement.

689

690

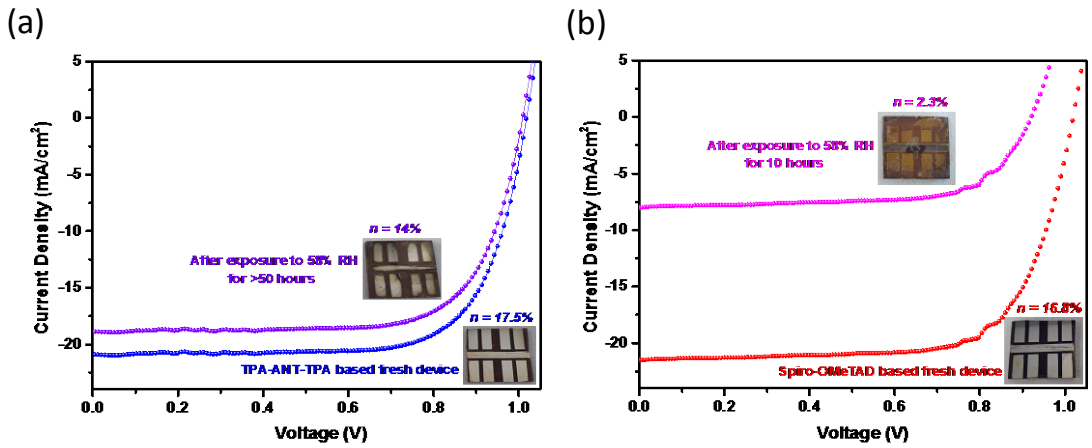

691

692 **Figure 4.** Photovoltaic performance of TPA-ANT-TPA (a) and Spiro-OMeTAD (b) based
693 $CH_3NH_3PbI_3$ PSC devices respectively on aging in humidity ≥ 58% (the fresh and aged PSC
694 devices shown in satellite pictures); Stability test/aging for 50 hours: without encapsulation
695 for, TPA-ANT-TPA and Spiro-OMeTAD based $CH_3NH_3PbI_3$ PSC devices at RH ≥
696 58%, After each consecutive measurement, the PSCs are kept in an ambient humidity setup
697 of RH ≥ 58%, Temperature = 22 ^oC, in dark condition. Grey colour scale represents humid
698 condition RH ≥ 50 %, Temperature = 22 ^oC, in dark condition.

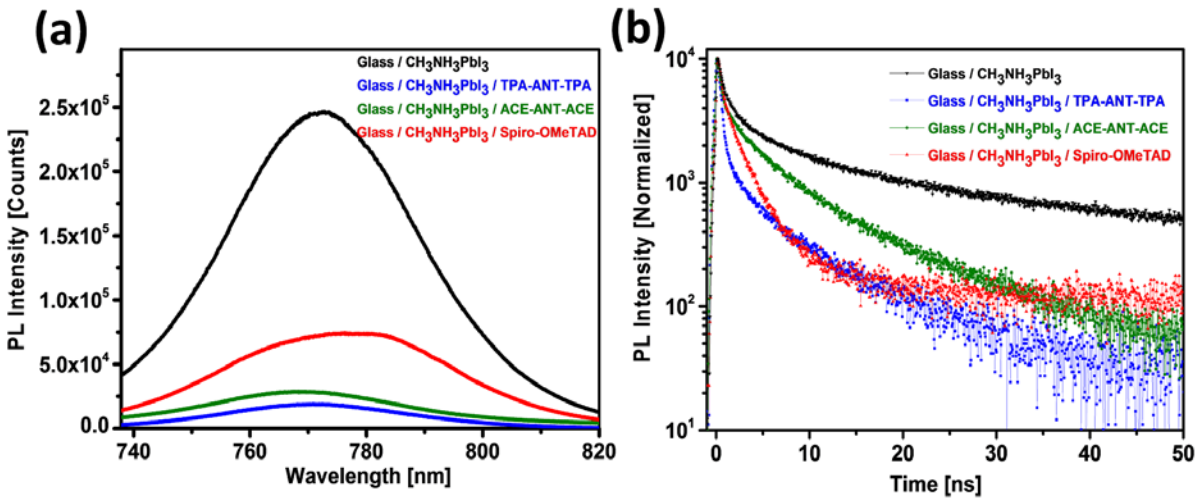

699

700 **Figure 5.** (a) Steady state Photoluminescence (PL) measured on bare perovskite film (black),
701 and hole transport layer deposited on the perovskite. Red, green, and blue curves represent
702 Spiro-OMeTAD, ACE-ANT-ACE, TPA-ANT-TPA, respectively, deposited on perovskite.
703 (b) Time resolved PL taken at excitation wavelength of 765 nm of the perovskite films with
704 different hole transport layers. A 5 mW picosecond pulsed diode laser at 635 nm excited on
705 the perovskite and hole transport layer side.

706
707

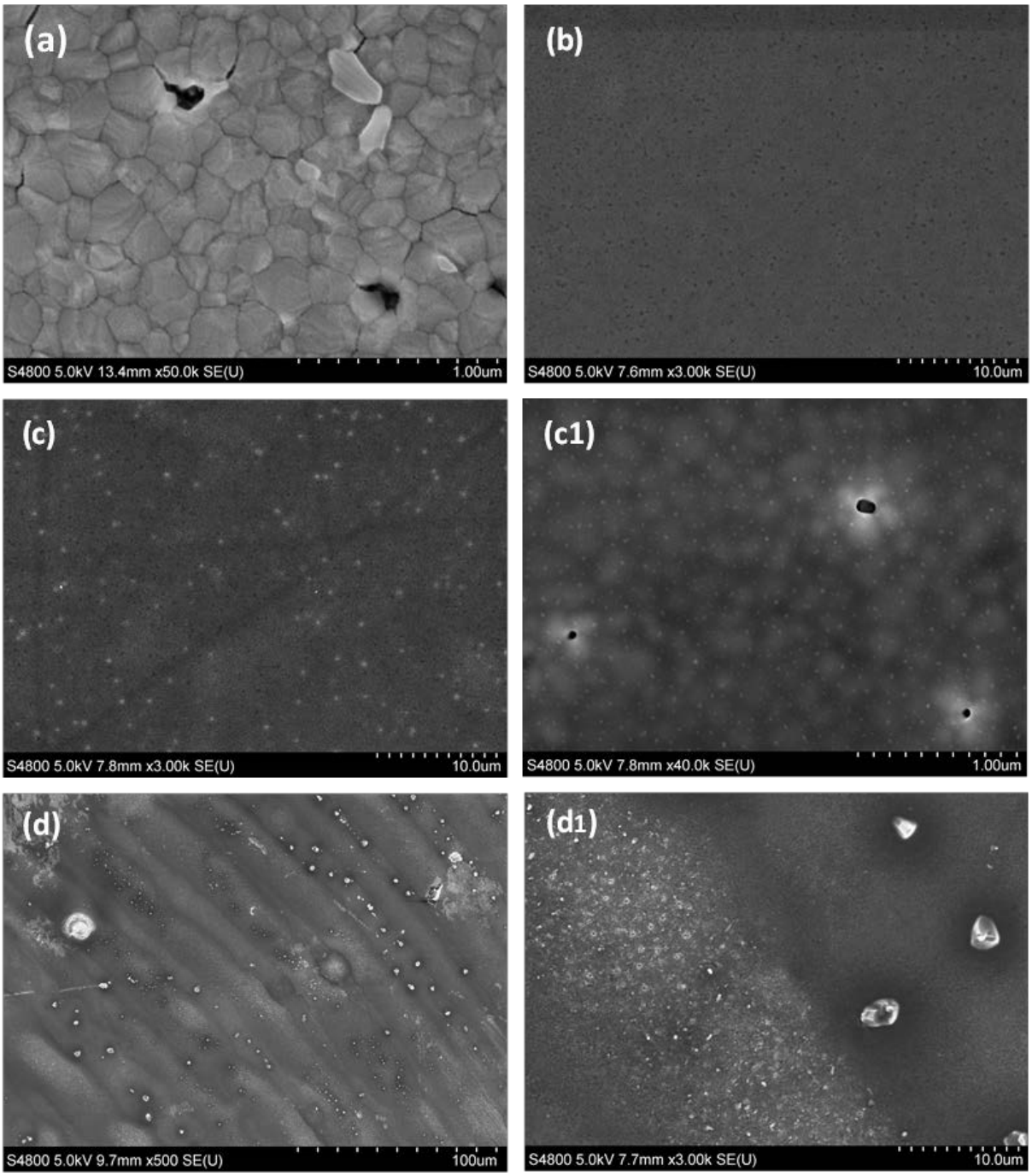

708

709 **Figure 6.** (a) Surface image of perovskite films deposited on top of FTO/compact
710 TiO_2/mesoporous TiO_2; (b) Top view of TPA-ANT-TPA on a perovskite layer; (c), and (c1)
711 top view of ACE-ANT-ACE on a perovskite layer; (d) and (d1) top view of Spiro-OMeTAD
712 on a perovskite layer.

713

Table 1. Thermal, optical and electrochemical properties of ACE-ANT-ACE and TPA-ANT-TPA

HTMs	λ_{max} [nm]		λ_{PL} [c)]	E_g^{opt} [d)]	E_{HOMO} [e)]	E_{LUMO} [e)]	E_{HOMO} [f)]	T_d	T_m
	Solution[a)]	Film[b)]	[nm]	[eV]	[eV]	[eV]	[eV]	[°C]	[°C]
ACE-ANT-ACE	461	467	480	2.56	-5.32	-2.76	-5.28	265	215
TPA-ANT-TPA	465	473	553	2.48	-5.41	-2.93	-5.40	290	256

[a)]Absorption spectrum was measured in chloroform (CF) solution; [b] Film was prepared by spin-coating an CF solution containing the sample onto glass substrate at a spin speed of 1000 rpm at room temperature; [c]Emission spectrum was analysed in CF solution; [d]Optical bandgap was calculated from the formula of $1240/\lambda_{onset}$; [e]The oxidation potential was also measured by photoelectron spectroscopy in air (PESA); $E_{LUMO}^{PESA}=E_{HOMO}^{PESA}+E_g^{opt}$; [f] Oxidation potential of the material was characterized in dichloromethane with 0.1 M tetrabutylammonium hexafluorophosphate at scan speed 100 mV/s, potentials vs. Fc/Fc^+.

Table 2. Summary of champion as well average photovoltaic performance and hole mobility of PSC devices prepared with different HTLs as ACE-ANT-ACE, TPA-ANT-TPA and Spiro-OMeTAD.[a)]

HTLs	Scan Direction	V_{OC} [V]	J_{SC} [mA/cm^2]	FF [%]	PCE [%]	Hole mobility [cm^2 V^{-1} s^{-1}]
ACE-ANT-ACE[b)]	Forward	1.03	18.7	67.1	13.1	2.4 x 10^{-5}
	Reverse	1.03	17.9	65.3	12.7	
	Average[d)]	0.99	17.8	65	11.4	
TPA-ANT-TPA[b)]	Forward	1.03	21.07	79.6	17.5	2.6 x 10^{-4}
	Reverse	1.03	21.05	79.6	17.5	
	Average[d)]	1.00	21.03	76.5	16	
Spiro-OMeTAD[c)]	Forward	1.04	21.09	76.8	16.8	1.5 x 10^{-4}
	Reverse	1.04	21.08	76.8	16.8	
	Average[d)]	0.98	20.0	70.2	13.8	

[a)]Cell size (active area): 0.100 cm^2. Photovoltaic performance at 1000 wm^{-2} (AM1.5G) and constant scan speed of 0.1 V/s mesoscopic $CH_3NH_3PbI_3$ devices; [b)]without additives; [c)]with additives: 4-tert-butylpyridine (*t*BP) and Li-bis(trifluoromethanesulfonyl)-imide (LiTFSI); [d)]An average device efficiency of total 81 devices.

731 **Table 3.** Comparison of lab synthesis costs of TPA-ANT-TPA and Spiro-OMeTAD.

Compound	Material cost [$/g]	Commercial price [$/g]
TPA-ANT-TPA	67	-
Spiro-OMeTAD	91.67[53, 55]	170-475[53, 55]

732

733

Table 4. The comparison of small molecular triphenylamine derivatives based dopant-free HTMs[a)]

HTM	HOMO [eV]	Hole mobility [$10^{-4}cm^2V^{-1}s^{-1}$]	Active area [cm^2]	V_{oc} [V]	J_{sc} [$mAcm^{-2}$]	FF [%]	PCE [%][e)]	Stability test[g)]	References
TPA-ANT-TPA[b)]	-5.41	2.6	0.1	1.03	21.07	79.6	17.5 (16.8)[f)]	80% (14%)[h)]	This study
1[b)]	-5.00	6.0	0.16	0.971	19.3	72	13.4 (15)	-	[45]
Z34[b)]	-5.14	7.46	0.16	1.053	21.27	69	15.9 (16.7)	100% (85%)	[33]
TPB-2-MOTPA[b)]	-5.28	0.77	-	0.927	17.37	69	11.06 (13.28)	99% (92%)	[56]
MeO-BPZTPA[b)]	-5.29	4.80	0.1	0.917	16.89	66.9	10.36 (13.65)	-	[57]
TAE-1[b)]	-5.32	0.592	-	0.885	17.22	72.2	11.02% (13.53%)	-	[58]
H101[b)]	-5.09	-	0.2	0.99	20.11	59	11.03% (13.7%)	-	[40]
EDOT-OMeTPA[b)]	-5.28	-	0.0831	0.95	18.9	61	11% (11.9%)	90% (90%)	[53]
OMeTPA-FA[b)]	-5.14	3.67	0.16	0.905	19.42	63	11.07% (14.68%)	88% (89%)	[59]
HTM2[b)]	-5.23	12.7	0.08	0.921	18.1	68	11.63% (12.08%)	-	[60]
2TPA-2-DP[c)]	-4.96	1.09	0.08	0.974	18.8	70.7	12.96% (11.46%)	-	[61]
Me-QTPA[c)]	-5.25	-	0.1	0.917	14.58	67.8	9.07% (13.65%)	100% (38%)	[62]
apv-EC[c)]	-5.28	7.23	0.08	0.932	18.4	70	12.0% (13.1%)	-	[63]
ST1[d)]	-5.24	4.57	0.16	1.059	21.07	66	15.4 (16.3)	85% (63%)	[64]
TPA-CN[d)]	-5.38	1.1	0.16	1.09	20.85	77	17.5 (19.2)	-	[35]
TP1[d)]	-5.18	0.441	0.16	0.956	20.23	63	12.63 (14.93)	70% (52%)	[65]
TBPC[d)]	-5.33	4.04	0.08	0.942	19.32	72	13.10% (13.28%)	-	[66]
Z1011[d)]	-5.21	8.49	0.16	1.096	20.52	70	16.3 (16.5)	97% (30%)	[32]
Z1013[d)]	-5.14	6.67	0.16	1.027	21.33	70.2	15.4 (16.7)	- (60%)	[34]

[a)]Device structure: FTO/compact TiO_2/mesoporous TiO_2/$CH_3NH_3PbI_3$/HTM/Cathode; photovoltaic parameters of the solar cells with HTMs evaluated under 1 sunlight illumination (100 mW cm^{-2}) condition.

[b)]TPA with OMe used as end-capping groups

[c)]TPA without OMe used as end-capping groups

[d)]TPA used as the central core

[e)]The best PCE of the HTMs based devices

[f)]The best PCE of standard doped SPIRO-OMeTAD

[g)]The percentage of the retaining performance after the ageing test (unsealed devices, at room temperature)

[h)]The percentage of the retaining performance of standard SPIRO-OMeTAD

Table of Content Figure

First time a low cost anthanthrone dye based hole transporting materials **ACE-ANT-ACE** and **TPA-ANT-TPA** end capped with dihydroacenaphthylene and triphenyleamine groups were designed and synthesized respectively. Among both, dopant-free **TPA-ANT-TPA** cut-rate HTM ($67/g) exhibits higher performance with 17.5% efficiency and retains respectable performance after 50 hours in 58% relative humidity than conventional expensive SPIRO-OMeTAD.

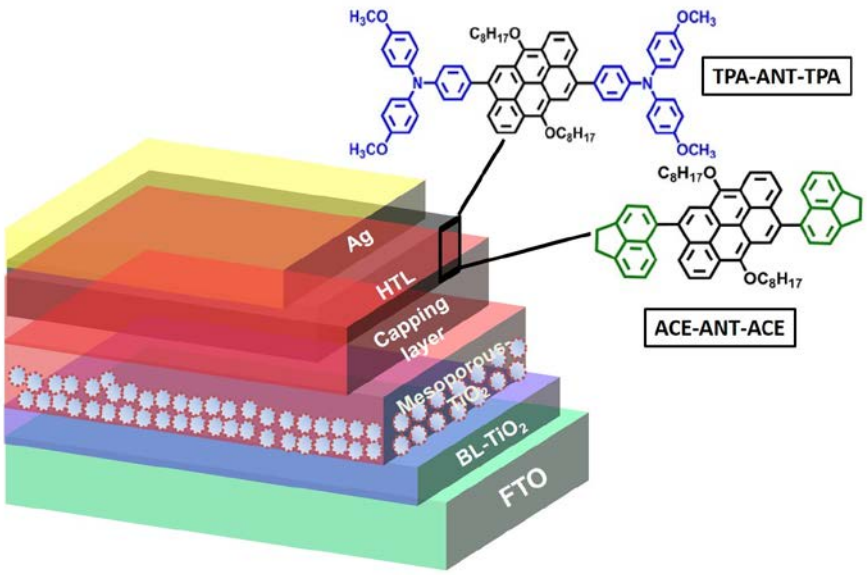

Supporting Information

Molecular Engineering Using an Anthanthrone Dye for Low Cost Hole Transport Materials: A Strategy for Dopant Free, High Efficiency Perovskite Solar Cells

Hong Duc Pham,[a♦] Thu Trang Do,[a] Jinhyun Kim,[b] Cecile Charbonneau,[c] Sergei Manzhos,[d] Krishna Feron,[e, f] Wing Chung Tsoi,[c] James R. Durrant,[b,c] Sagar M. Jain,[c♦*] Prashant Sonar[a*]

[a]Institute of Future Environment and School of Chemistry, Physics and Mechanical Engineering, Queensland University of Technology (QUT), 2 George Street, Brisbane, QLD-4001, Australia

[b]Department of Chemistry and Centre for Plastic Electronics, Imperial College London, Exhibition Road, London SW7 2AZ, United Kingdom

[c]SPECIFIC, College of Engineering, Swansea University Bay Campus, Fabian Way, SA1 8EN Swansea, United Kingdom

[d]Department of Mechanical Engineering, Faculty of Engineering, National University of Singapore

[e]CSIRO Energy Centre, NSW-2304, Australia.

[f]Centre for Organic Electronics, University of Newcastle, Callaghan, NSW 2308, Australia

♦ These authors contributed equally to the work

Corresponding author contact information

Prashant Sonar*, sonar.prashant@qut.edu.au

Sagar M. Jain*, s.m.jain@swansea.ac.uk

Content

824

836

Experimental details

1. Materials and Instruments

All chemicals and reagents were purchased from commercial company and used directly without any further purification. Synthesized compounds were characterized by ^{1}H-NMR and ^{13}C-NMR spectrum, which were obtained with a Varian-400 spectrometer or a Bruker 600 MHz spectrometer. High-resolution mass spectra were acquired on an LTQ Orbitrap Elite mass spectrometer (Thermo Fisher Scientific, Bremen, Germany) equipped with an electrospray ionisation (ESI) source, operating in the positive ion mode at a resolution of 120,000 (at *m/z* 400). Reserpine ($[M+H]^+$, *m/z* 609.28066) was used as a lock mass calibrant to increase the measurement accuracy. Thermal analysis was performed using a Pegasus Q500TGA thermogravimetric analyzer under nitrogen atmosphere at a heating rate of 10 ^{o}C/min. Differential scanning calorimetry (DSC) was conducted under nitrogen using a Chimaera instrument Q100 DSC. The sample was heated at 10 ^{o}C/min from 30 ^{o}C to 300 ^{o}C. Absorption spectra were recorded on a Shimadzu UV-1800 spectrometer. Photoelectron spectroscopy in air (PESA) measurements were conducted using on an AC-2 photoelectron spectrometer (Riken-Keiki Co.). The cyclic voltammetry (CV) was performed by a Potentiostat Galvanostat with a three electrode cell in a solution of Bu_4NPF_6 (0.1M) in freshly distilled DCM at a scan rate of 100 mV/s. The counter electrode was a Pt wire, the working electrode was glassy carbon and an Ag/Ag+ electrode was used as the reference electrode.

2. Synthesis

Synthesis of 4-bromo-*N*,*N*-bis(4-methoxyphenyl)aniline (**2**)

Compound **1** (2 g, 11.6 mmol), 1-iodo-4-methoxybenzene (5.97 g, 25.5 mmol.), KOH (5.1 g, 90.5 mmol), CuCl (0.05 g, 0.5 mmol) and 1,10-phenanthroline monohydrate (0.1 g, 0.5 mmol) were dissolved in anhydrous toluene. After being degassed by argon for 20 min, the reaction mixture was heated at 120 °C overnight. Then the mixture was cooled to room temperature (RT). Excessive potassium hydroxide (KOH) was neutralized by water. After that, the mixture was extracted by dichloromethane (DCM). The organic layer was dried over anhydrous sodium sulphate (Na_2SO_4) and concentrated by evaporation. The crude product was purified by silica gel chromatography using a mixture of hexane and DCM as eluent to obtain product as a white crystal (2.5 g, 56%). ^{1}H NMR (600 MHz, $CDCl_3$, ppm): δ 7.16 (d, *J* = 9.0 Hz, 2H), 6.95 (d, *J* = 8.4 Hz, 4H), 6.75 (d, *J* = 8.4 Hz, 4H), 6.72 (d, *J* = 8.4 Hz, 2H), 3.72 (s, 6H).

Synthesis of 4-methoxy-*N*-(4-methoxyphenyl)-*N*-(4-(4,4,5,5-tetramethyl-1,3,2-dioxaborolan-2-yl)phenyl)aniline (**3**)

In a Schlenk flask, compound **2** (2.5 g, 6.5 mmol) was mixed with diborane pinacol ester (2.5 g, 9.8 mmol), KOAc (1.9 g, 19.6 mmol) and Pd(dppf)Cl_2 (1.2 g, 1.6 mmol) in 50 mL dimethylformamide (DMF). Then, the mixture was heated overnight at 80 °C. After cooling to RT, the reaction mixture was extracted by chloroform (CF) and water. Subsequently, it was dried over anhydrous Na_2SO_4 and then concentrated by evaporation. The residue was purified by silica gel chromatography using a mixture of hexane and DCM as eluent to obtain product as a white crystal (1.8 g, 64%). ^{1}H NMR (600 MHz, $CDCl_3$, ppm): δ 7.53 (d, *J* = 7.2 Hz, 2H), 6.98 (m, 4H), 6.78-6.74 (m, 6H), 3.72 (s, 6H), 1.24 (s, 12H).

Synthesis of 4,10-dibromo-6,12-bis(octyloxy)anthanthrene (**5)**

Compound **4** (2.0 g, 4.3 mmol), aqueous sodium hydroxide (0.2 M, 20 mmol), Aliquat 336 (2.1 g, 5.2 mmol), sodium dithionite (1.9 mg, 11.1 mmol), and 1-bromooctane (6.6 g, 34.3

mmol) were added into a round bottom flask and then degassed by argon for 20 min. The mixture was stirred at 80 °C overnight. The crude component was extracted by water and methanol. The organic layer was dried over anhydrous Na_2SO_4 and concentrated by evaporation. Purification by using column chromatography yielded the main product as an orange solid (2.4 g, 80%). ^{1}H NMR (400 MHz, $CDCl_3$, ppm): δ 8.78-8.75 (m, 4H), 8.63 (d, *J* = 7.6 Hz, 2H), 8.22-8.18 (t, *J* = 8.0 Hz, 2H), 4.34-4.31 (t, *J* = 6.4 Hz, 4H), 2.15 (m, 4H), 1.76 (m, 4H), 1.37-1.24 (m, 16H), 0.94-0.91 (t, *J* = 6.8 Hz, 6H).

Synthesis of 2-(1,2-dihydroacenaphthylen-5-yl)-4,4,5,5-tetramethyl-1,3,2-dioxaborolane (**6**) : Into a Schlenk flask, commercially available 5-bromo-1,2-dihydroacenaphthylene (2.89 g, 12.4 mmol) was mixed with diborane pinacol ester (3.29 g, 13 mmol), KOAc (3.31 g, 33.6 mmol) and Pd(dppf)Cl_2 (271 mg) in 80 mL dioxane. Then, the mixture was heated overnight at 80°C . After cooling to RT, the reaction mixture was extracted by chloroform (CF) and water. Subsequently, it was dried over anhydrous magnesium sulphate and then concentrated by evaporation. The residue was purified by silica gel chromatography using a mixture of hexane and ethyl acetate as eluent to obtain product 2-(1,2-dihydroacenaphthylen-5-yl)-4,4,5,5-tetramethyl-1,3,2-dioxaborolane (**6**) as a white powder (1.8 g, 51%). 1H NMR (400 MHz, CDCl3, ppm): δ 8.36 (d, *J* = 8.4 Hz, 1H), 8.04-8.02 (d, *J* = 6.8 Hz, 1H), 7.50-7.47 (m, 1H), 7.29-7.27 (d, *J* = 7.2 Hz, 2H), 3.38 (s, 4H), 1.40 (s, 12H).

Synthesis of 4,10-bis(1,2-dihydroacenaphthylen-5-yl)-6,12-bis(octyloxy)-6,12-dihydronaphtho[7,8,1,2,3-*nopqr*] tetraphene (**ACE-ANT-ACE**)

In a round bottom flask, compound **5** (200 mg, 0.290 mmol), compound **6** (245 mg, 0.875 mmol), and 2M aqueous K_2CO_3 solution (12 mL) were dissolved in degassed toluene (18 mL). The solution was purged with argon for 15 minutes, then tetrakis(triphenylphosphine)palladium (16.18 mg 0.014 mmol) was added. The reaction was

stirred at 120 °C for 2 days. After the reaction mixture was cooled to room temperature and extracted with chloroform and water. The organic layer was dried over anhydrous Na_2SO_4 and concentrated by evaporation. The solvent was evaporated and the crude product recrystallized from hot acetone to yield the desired compound as a yellow solid (205 mg, 65%). ^{1}H NMR (400 MHz, $CDCl_3$, ppm): δ 8.81 (d, *J* = 8.0 Hz, 2H), 8.57 (s, 2H), 8.01-7.98 (t, *J* = 8.0 Hz, 2H), 7.92 (d, *J* = 7.2 Hz, 2H), 7.79 (d, *J* = 6.8 Hz, 2H), 7.55-7.54 (d, *J* = 7.2 Hz, 2H), 7.44-7.42 (m, 2H), 7.37-7.31 (m, 4H), 4.42-4.38 (t, *J* = 6.8 Hz, 4H), 3.58 (m, 8H), 2.08 (m, 4H), 1.63 (m, 4H), 1.26 (m, 16H), 0.88-0.84 (t, *J* = 6.8 Hz, 6H). ^{13}C NMR ($CDCl_3$, ppm): δ 149.55, 146.20, 146.12, 139.47, 137.96, 134.18, 132.25, 131.40, 129.74, 129.68, 127.95, 125.93, 125.71, 124.38, 123.68, 123.90, 121.90, 121.66, 120.47, 120.05, 119.48, 119.31, 119.24, 31.79, 30.71, 30.31, 29.52, 29.28, 26.19, 22.65, 14.10. ESI-MS: $C_{62}H_{60}O_2^{+\bullet}$ m/z 836.4587 (calculated *m/z* 836.4588).

Synthesis of 4,4'-(6,12-bis(octyloxy)-6,12-dihydronaphtho[7,8,1,2,3-*nopqr*]tetraphene-4,10-diyl)bis(*N*,*N*-bis(4-methoxyphenyl)aniline) (**TPA-ANT-TPA**)

In a round bottom flask, compound **5** (200 mg, 0.290 mmol), compound **3** (313 mg, 0.725 mmol), and 2M aqueous K_2CO_3 solution (12 mL) were dissolved in degassed toluene (18 mL). The solution was purged with argon for 15 minutes, then tetrakis(triphenylphosphine)palladium (16.18 mg 0.014 mmol) was added. The reaction was stirred at 120 °C for 2 days. After the reaction mixture was cooled to room temperature and extracted with chloroform and water. The organic layer was dried over anhydrous Na_2SO_4 and concentrated by evaporation. The solvent was evaporated and the crude product recrystallized from hot acetone to yield the desired compound as a yellow solid (200 mg, 60%). ^{1}H NMR (400 MHz, $CDCl_3$, ppm): δ 8.81 (d, *J* = 8.0 Hz, 2H), 8.41 (s, 2H), 8.38 (d, *J* = 7.2 Hz, 2H), 8.14-8.10 (t, *J* = 8.0 Hz, 2H), 7.60 (d, *J* = 8.8 Hz, 4H), 7.25-7.21 (m, 8H), 7.15 (d, *J* = 8.4 Hz, 4H), 6.92 (m, 8H), 4.40-4.37 (t, *J* = 6.8 Hz, 4H), 3.83 (s, 12H), 2.14 (m, 4H),

1.72 (m, 4H), 1.31 (m, 16H), 0.90-0.87 (t, J = 6.4 Hz, 6H). ^{13}C NMR (100 MHz, $CDCl_3$, ppm): δ 155.97, 148.27, 140.87, 139.72, 132.72, 131.54, 130.65, 126.91, 126.00, 125.96, 125.59, 124.38, 123.11, 122.19, 121.89, 120.40, 119.85, 119.73, 114.76, 55.51, 31.87, 30.80, 29.71, 29.61, 29.36, 26.35, 22.69, 14.16. ESI-MS: $C_{78}H_{78}N_2O_6^{+\bullet}$ m/z 1138.5857 (calculated *m/z* 1138.5854).

3. Substrates Preparation: A patterned FTO-coated glass (13 Ω sq^{-1}, Aldrich) was etched by Zn powder and 2 M HCl diluted in deionized water. Subsequently, the substrates were cleaned with detergent diluted in deionized water, rinsed with deionized water, acetone and ethanol, and dried with clean dry air. A compact blocking layer of TiO_2 (40 nm, c-TiO_2) was deposited on the fluorine doped SnO_2 (FTO, Pilkington, TEC8) substrate by spray pyrolysis using a 20 mM titanium di-isopropoxide bis(acetylacetonate) solution (Aldrich) at 500^{o}C for 30 minutes.[1] [50] [50] [50] [50] [50] [50] [50] [50] To deposit the mesoporous TiO_2 layer, Dyesol DSL 30 NR-D paste is dissolved in anhydrous isopropanol and kept for sonication for 1 hours. Once the solution is homogeneous it is ready to deposit on FTO/Compact TiO_2 substrate by spin coating at 3000 rpm for 30 second followed by annealing at 550^O C estimated to give ~400 nm thick layer.[2]

4. Fabrication of Devices: The PSCs were prepared by one step spin coating of a $CH_3NH_3PbI_3$ solution. The solution was prepared in DMF/DMSO = 6:4 by mixing CH_3NH_3I (0.199 gm) and PbI_2 (0.600 gm). The solution was heated at 60 ^{o}C for 3 hours for mixing. Then the solution was spin coated using Chlorobenzene as antisolvent at rpm of 4000 for 30 s, and annealed for 30 minutes at 100 ^{o}C on a hotplate. The absorber perovskite material with electrode (FTO/Compact-TiO_2/Mesoporous TiO_2) is ready after the above annealing procedure. The electrodes with the absorber material were allowed to cool down to room temperature. A solution containing 2-7,7-tetrakis(N,N-di-*p*-methoxyphenylamine)-9,9 17-

spirobifluorene (Spiro-OMe-TAD) in chlorobenzene and additives (10 µl ml^{-1} *t*BP, 32 µl ml^{-1} Li-TFSI solution: 600 Mm in acetonitrile) was spin coated onto the perovskite film at 5000 rpm, for 30 second. Finally, 80 nm thick silver contacts were evaporated at 10^{-4} torr.

Similarly, other hole transporting materials, TPA-ANT-TPA and ACE-ANT-ACE were dissolved in 60 mg in 1 ml chlorobenzene and kept for sonication for 30 minutes. The solution was filtered (0.45 ɯ) before use and spin coated on top of perovskite absorber at 5000 rpm for 30 seconds.

5. Power Conversion Efficiency and Incident Photon to Current Conversion Efficiency (IPCE): Masked devices (0.100 cm^2) were tested under a class AAA solar simulator (Newport Oriel Sol3A) at AM1.5 and 100 mW cm^{-2} illumination conditions calibrated against a KG5 filtered silicon reference cell (Newport Oriel 91150-KG5) using a Keithley 2400 source meter. Current–voltage sweeps were performed from forward-to-reverse bias at a rate of 0.1 V s^{-1}.

6. Stability Measurements: Humidity test : Stability tests on optimized champion devices without encapsulation for different hole transporting material were performed. The solar cells were kept in relative humidity of >580% at room temperature in the dark. The simple setup is shown in Figure S12.

Continuous 1 sun illumination: The non-encapsulated cells are placed in a cell holder with a glass cover and are in direct contact with ambient atmosphere. For the stability the cells are kept at 35^{o}C temperature, under 1sun illumination using Solar simulator class A 1.5 M at full sun under short circuit condition for 200 hours. IV curves were characterized by an electronic system using 22 bits delta-sigma analogic to digital converter. For IV curves measurement, a scan rate of 10 mV s^{-1} with a step of 5 mV was used, maintaining the temperature of the holder to 35^{o}C while the temperature of the cells was measured around 45^{o} C. The system

comprises a set of I–V curves at different light intensities (dark current, 10 and 100 mW cm^{-2}). Between each measurement the cells are maintained at the maximum power point using a MPPT algorithm under 100 mW cm^{-2}. A reference Si-photodiode is placed in the holder to verify the stability of the light. The same setup was used to do the aging of all three HTLs, which are covered on perovskite material (Figure S15).

7. Characterisation:

Scanning Electron Microscopy (SEM): high magnification observations of the hole transport materials and device cross sections were acquired using a Hitachi S-4800 field emission gun-scanning electron microscope (5 kV, WD-8 mm)

Photoluminiscence Measurements: Steady state emission measurements were done on the Horiba Fluoromax-4 spectroflurometer equipped with double-grating at the excitation wavelength of 550 nm on the 3-layer assembly Glass/$CH_3NH_3PbI_3$/HTM with different HTMs (TPA-ANT-TPA, ACE-ANT-ACE, and Spiro-OMeTAD). Front face illumination with respect to the incident beam was used to minimize the inner filter effects.

Contact Angle Measurements: Contact angle measurements were performed using a simple home built instrument. High resolution images of water droplets on the surface of hole transport layers deposited on the perovskite sample were collected using Nikon DSL90 camera, as shown in Figure S11.

Time Correlated Single Photon Counting (TCSPC): Time Correlated Single Photon Counting measurements were performed on Horiba Jobin Yvon Fluorolog system. Steady state photoluminiscence measurements were done on perovskite and hole transport layers with < 200 ps pulses of 635 nm excitation from a pisosecond diode laser (NanoLED source). The laser pulse excitation density was $2.3x10^{14}$ cm^{-3}, Rep.rate:1MHz. Measurements were done in reverse mode at 1 MHz rep. rate. A cutoff filter (OG575) was used to block the stray

excitation light. To increase the sensitivity of measurements, all wavelengths transmitted by cutoff filter were collected without the use of any monochromator.

Hole transport measurements : space charge limited current (SCLC) method

PEDOT: PSS (Poly(3,4-ethylendioxythiophene)–poly (styrene sulfonate)) was spin-coated onto indium tin oxide substrate (ITO) and dried at 130 ºC for 20 minutes in vacuum. The purpose of PEDOT: PSS layer (40 nm) was to reduce the roughness of ITO as well as to improve the work function, achieving enhanced hole-only device properties. The HTMs were spincoated onto PEDOT: PSS from chloroform solution (30 mg/mL) in a nitrogen atmosphere. Finally, Au contacts (400 nm thick) were applied via thermal evaporation through a shadow mask in 2 x 10^{-6} Torr vacuum. The work function of Au and ITO are close to the HOMO energy level of the HTM as well as far below the LUMO energy level. Therefore, the electron injection barrier is higher than the corresponding hole injection barrier. As a result, the transport is dominated by holes. The J–V characteristics of the sample was measured with a Keithley 2420 source meter unit at room temperature. The device configuration and equations to extract mobility has been reported by us previously.[3]

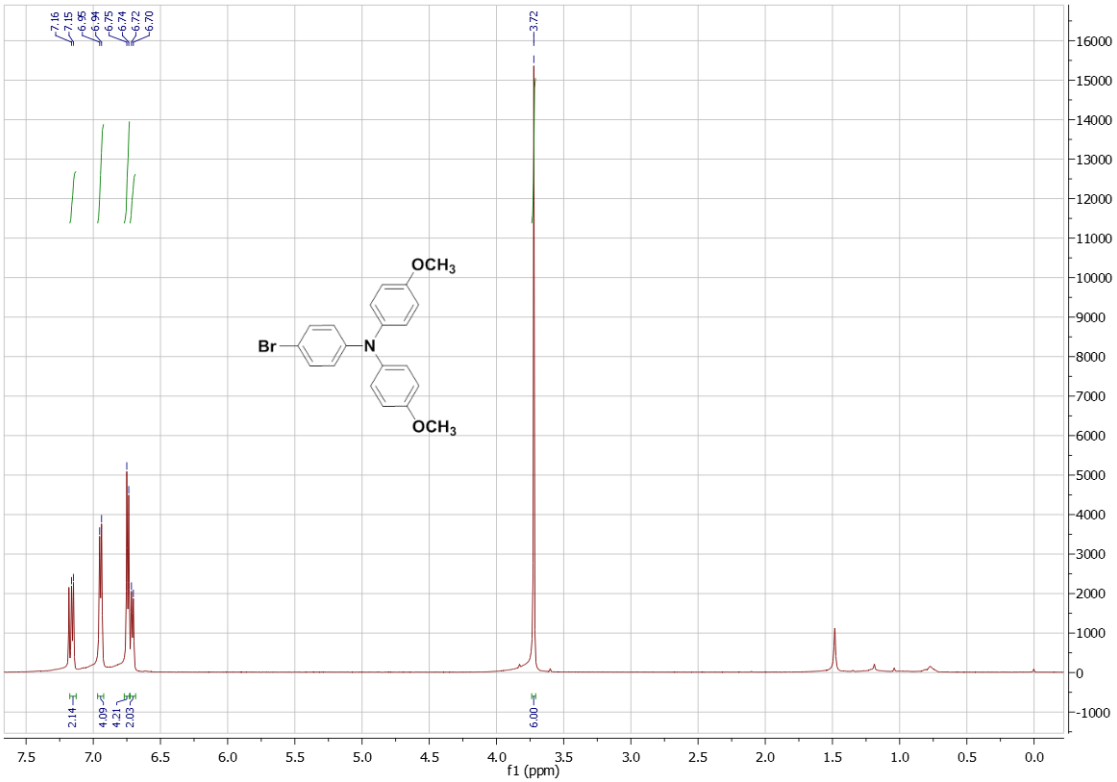

1023

1024 **Figure S1.** ^{1}H (600 MHz, $CDCl_3$) spectrum of 4-bromo-*N*, *N*-bis(4-methoxyphenyl)aniline
1025 (2).

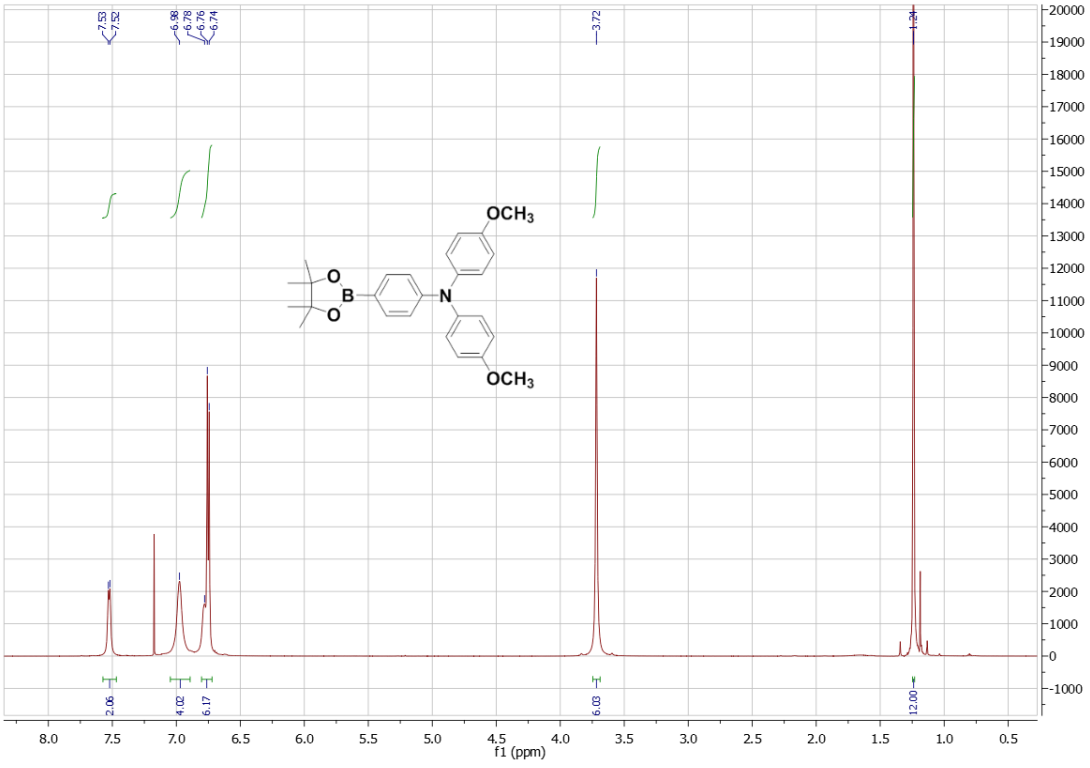

1026

1027 **Figure S2.** ^{1}H (600 MHz, $CDCl_3$) spectrum of 4-methoxy-*N*-(4-methoxyphenyl)-*N*-(4-
1028 (4,4,5,5-tetramethyl-1,3,2-dioxaborolan-2-yl)phenyl)aniline (3).

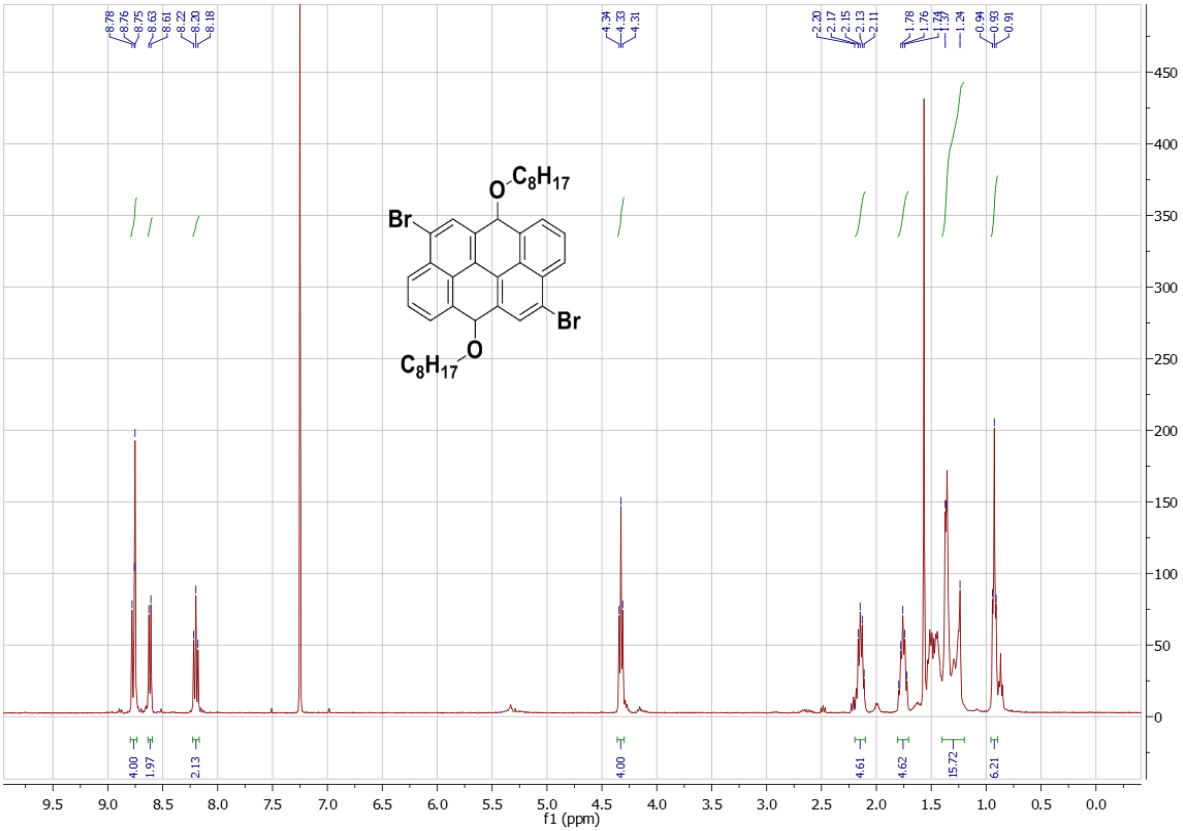

1029

1030 **Figure S3.** ^{1}H (400 MHz, $CDCl_3$) spectrum of 4,10-dibromo-6,12-bis(octyloxy)-6,12-
1031 dihydronaphtho[7,8,1,2,3-*nopqr*]tetraphene (5).

1032

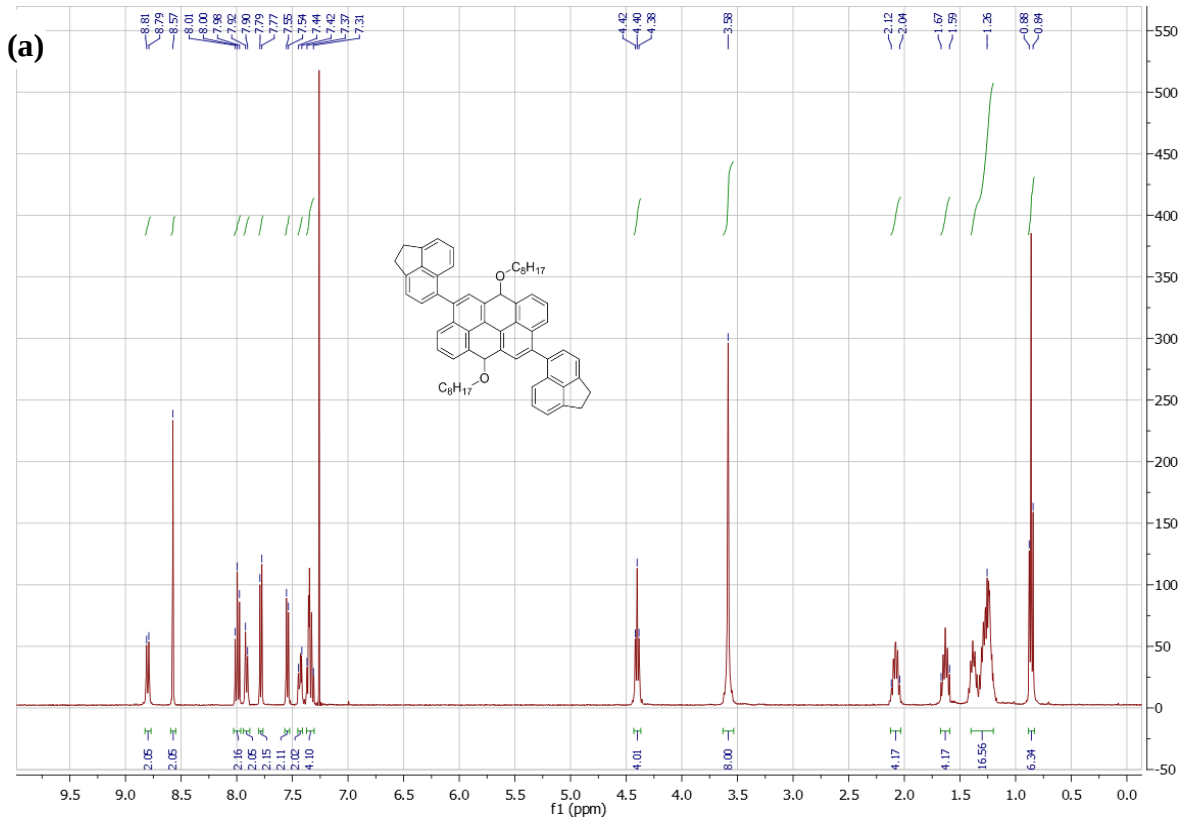

1033

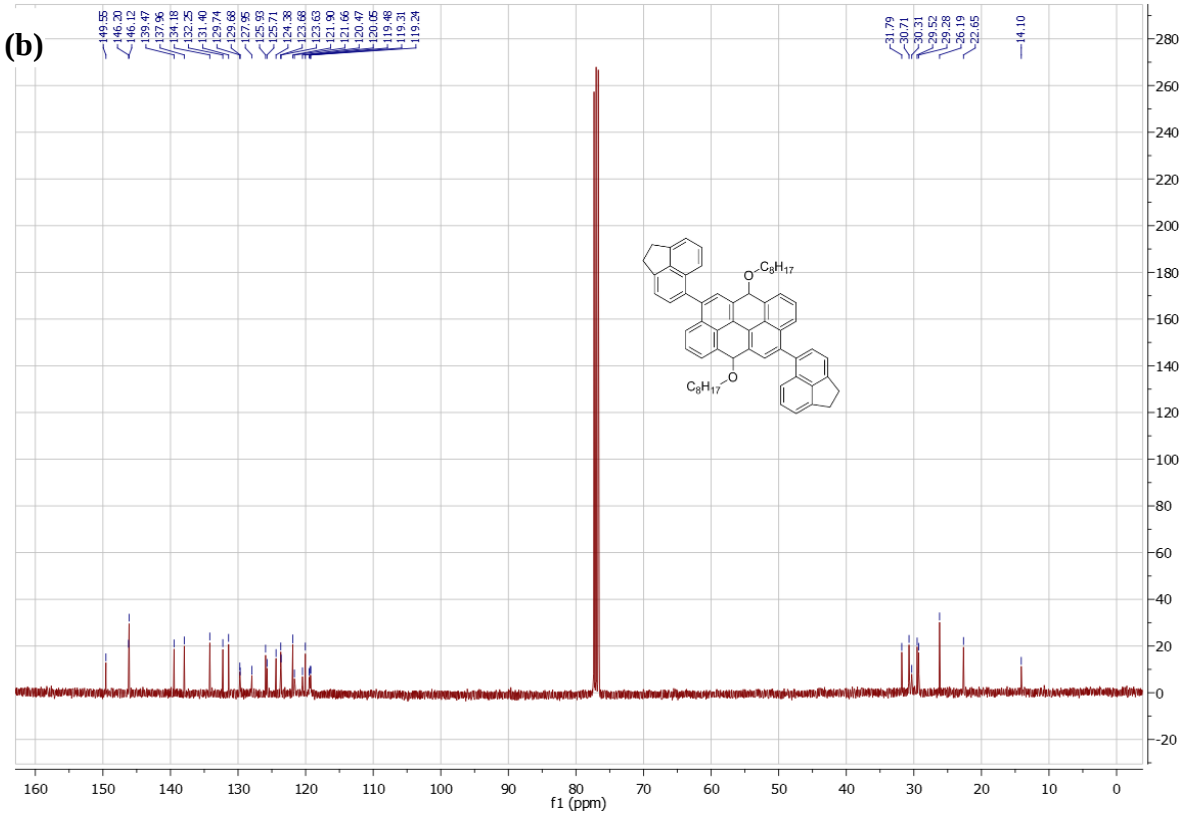

1034

1035 **Figure S4.** (a) ^{1}H (400 MHz, $CDCl_3$) spectrum and (b) ^{13}C NMR (100 MHz, $CDCl_3$)
1036 spectrum of ACE-ANT-ACE.

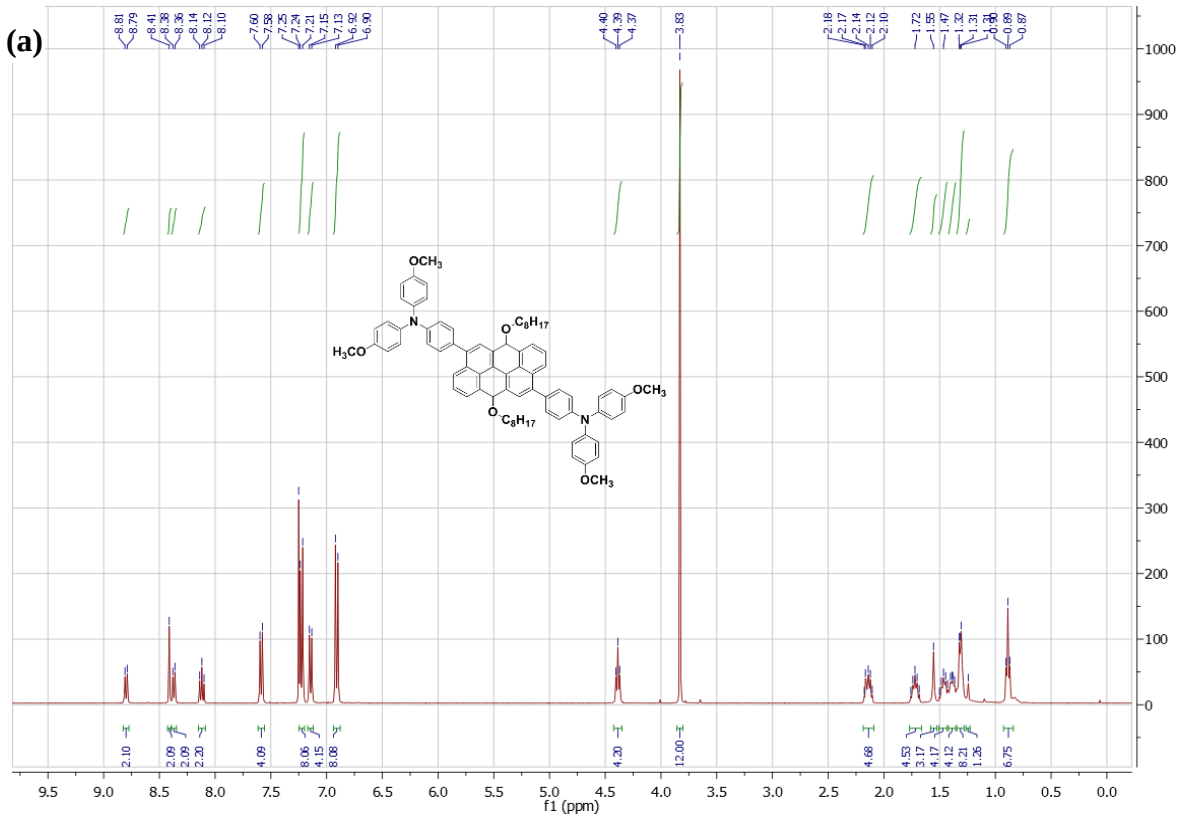

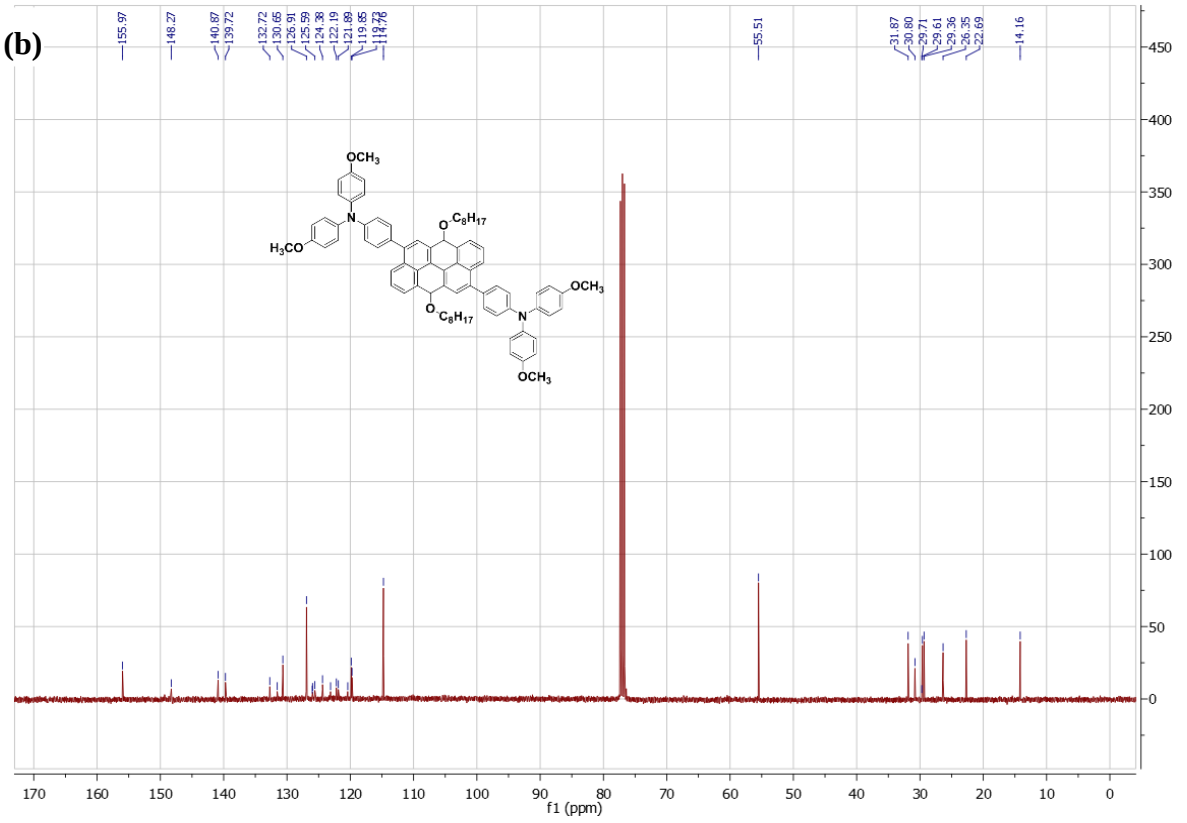

Figure S5. (a) ^{1}H (400 MHz, $CDCl_3$) spectrum and (b) ^{13}C NMR (100 MHz, $CDCl_3$) spectrum of TPA-ANT-TPA.

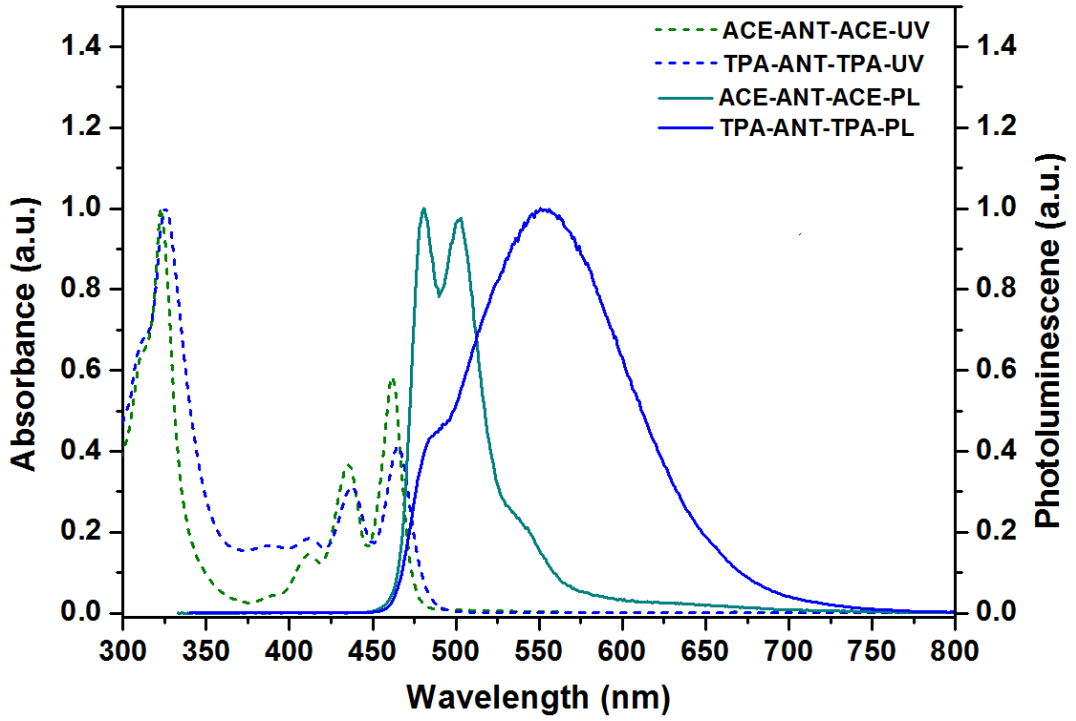

Figure S6. Normalised absorption and emission spectra of ACE-ANT-ACE and TPA-ANT-TPA in CF solution.

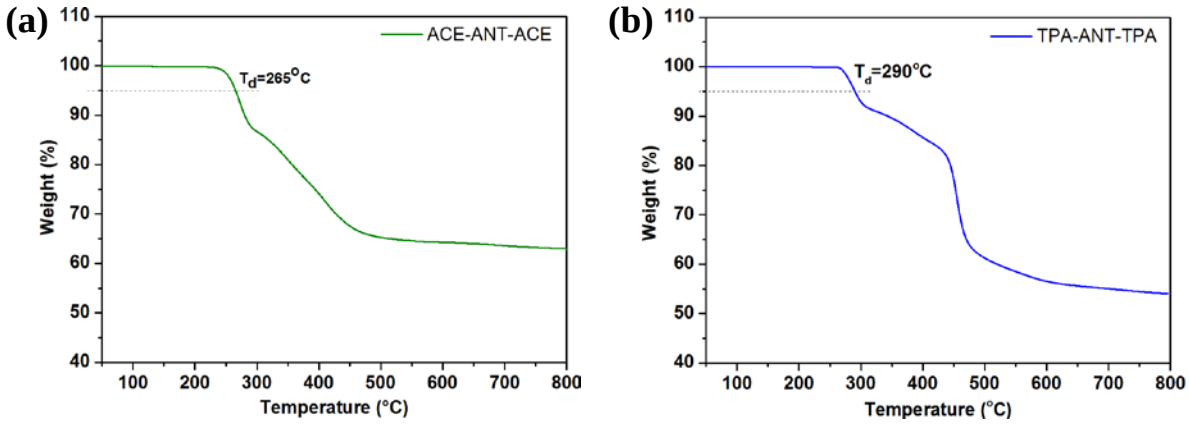

Figure S7. Thermogravimetric analysis (TGA) curve of (a) ACE-ANT-ACE and (b) TPA-ANT-TPA.

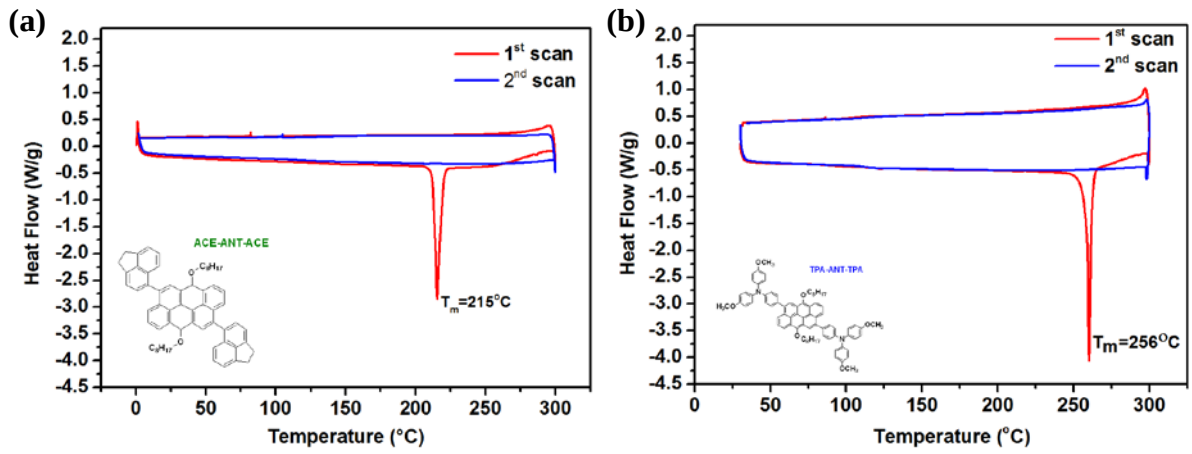

Figure S8. Differential scanning calorimetry (DSC) of (a) ACE-ANT-ACE and (b) TPA-ANT-TPA with scan rate of 10 °C/min under N_2 atmosphere.

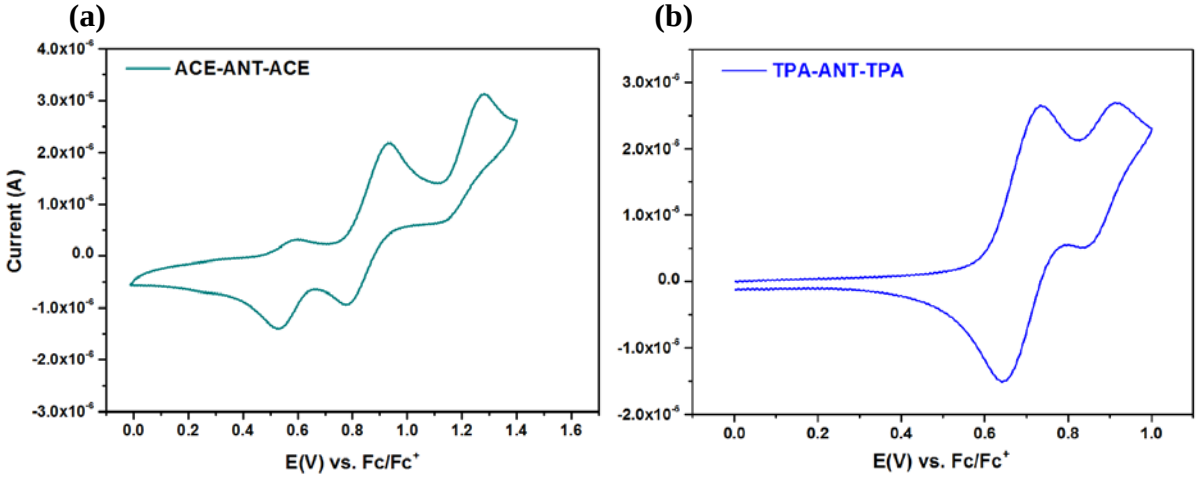

Figure S9. Cyclic voltammograms of (a) ACE-ANT-ACE and (b) TPA-ANT-TPA. The oxidation was measured in DCM/0.1M Bu_4NPF_6 at a scan rate of 100 mV/s.

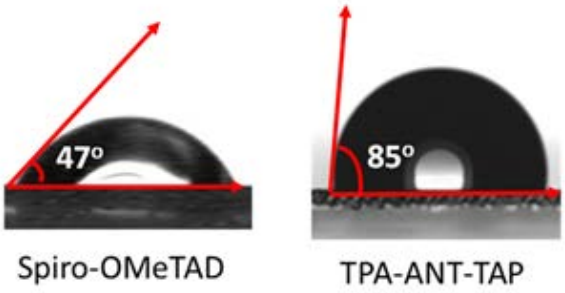

Figure S10. Contact angle measurements performed on Spiro-OMeTAD and TPA-ANT-TPA surface deposited on $CH_3NH_3PbI_3$.

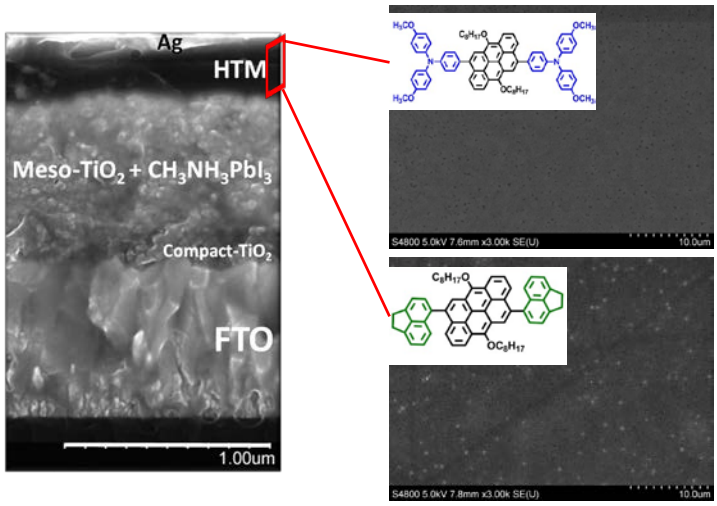

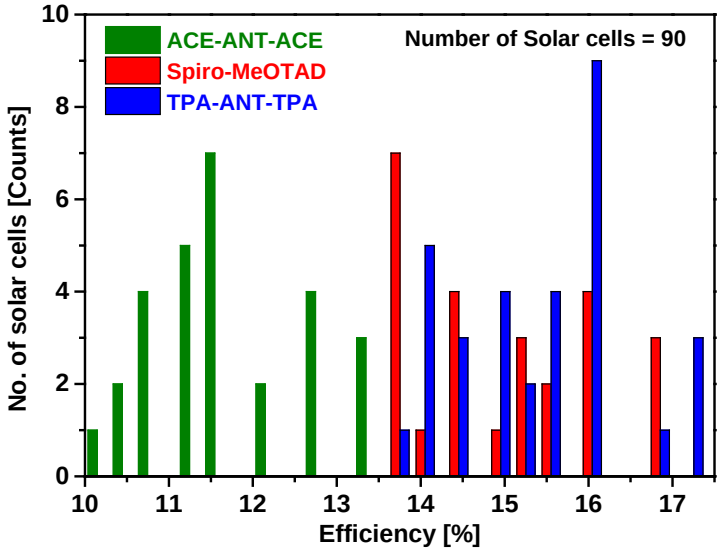

Figure S11. SEM cross sectional image of perovskite device with thin film morphology comparison of both HTM (upper) and statistics of 90 PSC devices prepared using (i) ACE-ANT-ACE (green bars); (ii) TPA-ANT-TPA (blue bars) and (iii) Spiro-OMeTAD (red bars) as hole transporting materials (lower)

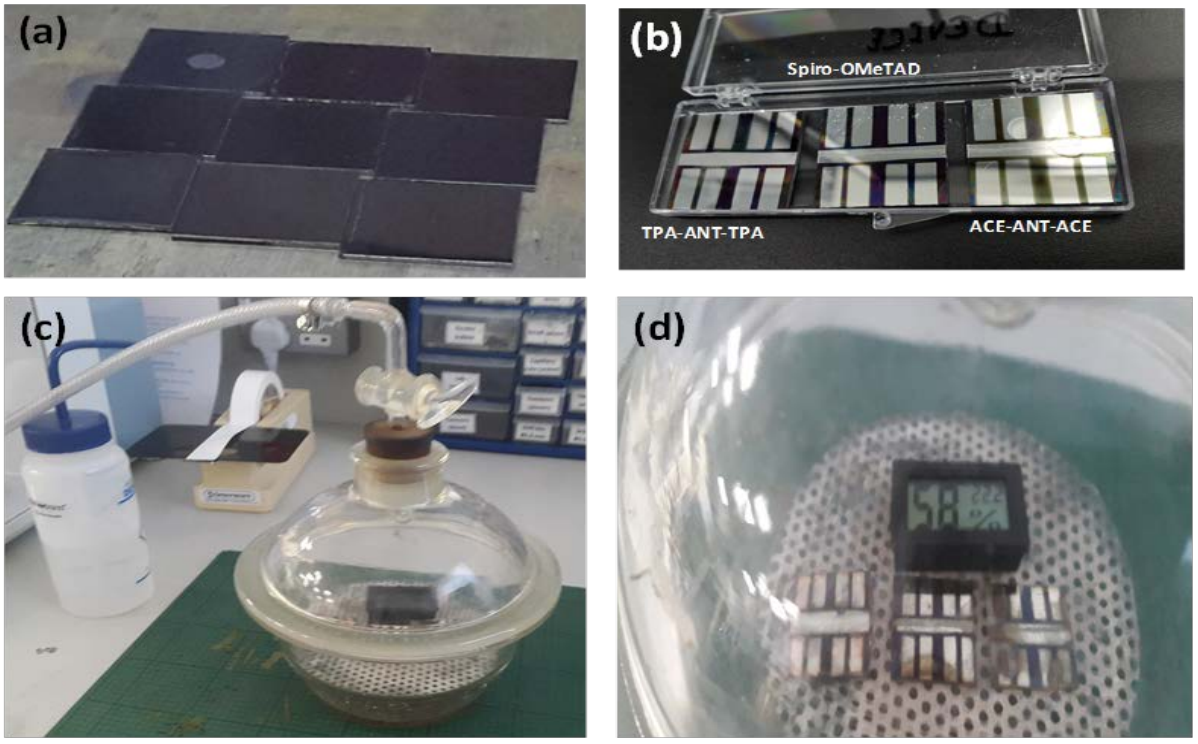

Figure S12. (a) FTO/Compact-TiO_2/Mesoporous TiO_2/$CH_3NH_3PbI_3$ assemblies after annealing; (b) Perovskite devices with 3 different hole transport layers; (c) and (d) Simple stability measurement setup in a humidified desiccator for aging of PSCs in the dark and in >50% humidity.

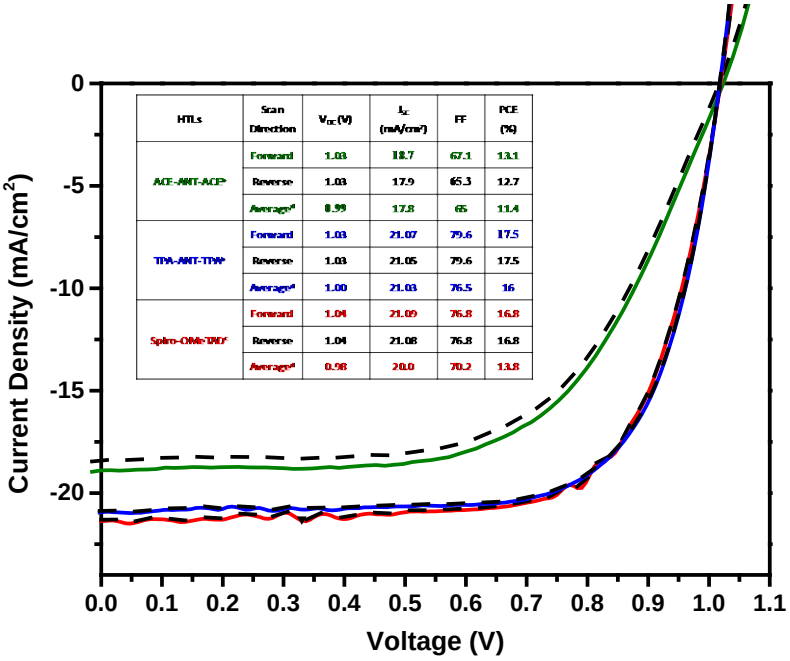

1080

1081 **Figure S13.** Hysteresis behaviour of champion solar cells made using TPA-ANT-TPA (blue
1082 curve) , ANT-ACE-ANT (green curve) and Spiro-OMeTAD (red curve) as HTLs. Scan from
1083 0 V to V_{oc} at a constant scan speed of 0.1 V/s. Device performance parameters represented in
1084 the insert table.

1085

1086

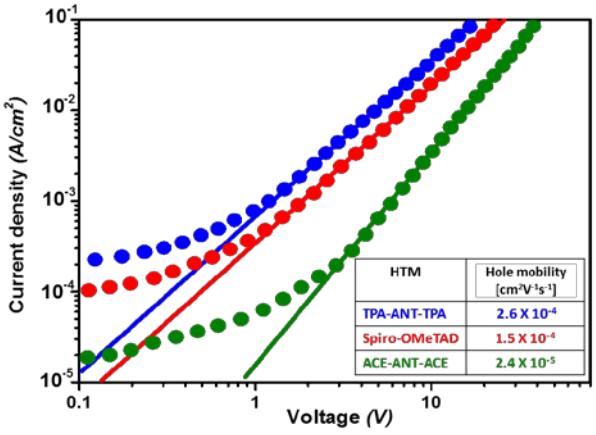

1087

1088

1089 **Figure S14.** J-V data for space charge limited current (SCLC) method of hole-mobility
1090 determination. The resulting mobilities of TPA-ANT-TPA (blue line), ACE-ANT-ACE
1091 (green line) and Spiro-OMeTAD (red line) were 2.6 x 10^{-4}, 2.4 x 10^{-5}, 1.5 x 10^{-4} $cm^2V^{-1}s^{-1}$
1092 respectively.

1093

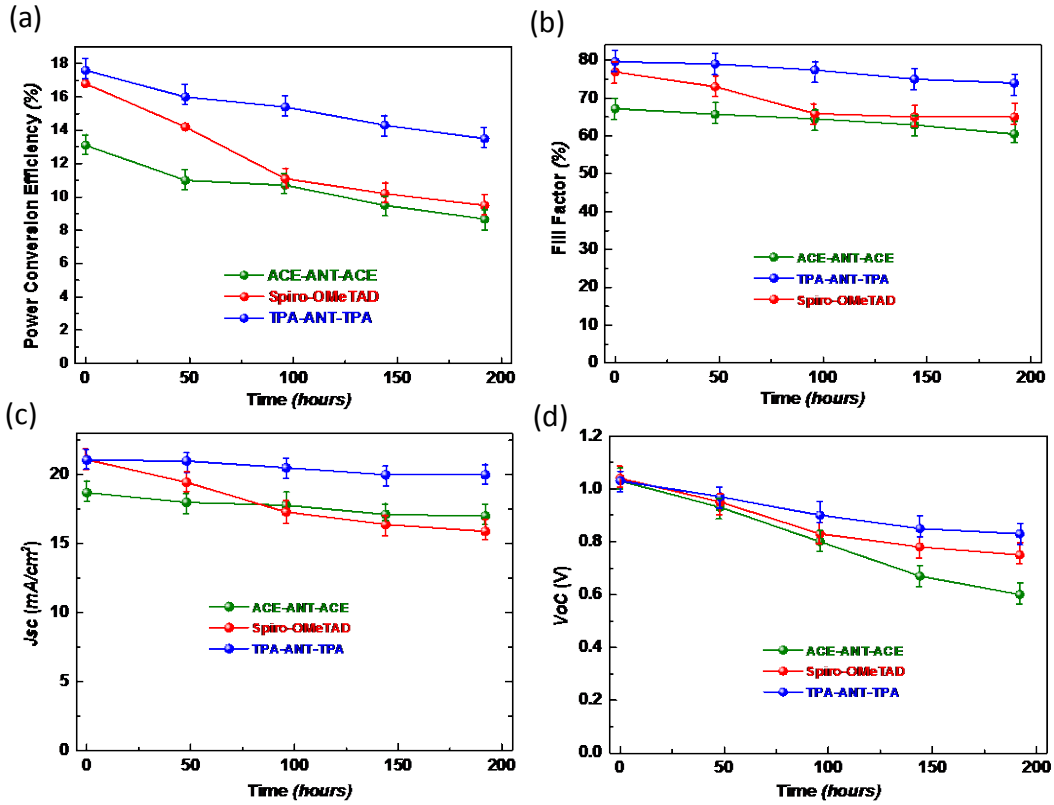

Figure S15. Stability measurements of champion devices under continuous 1 sun, AM 1.5 G illuminations and at short circuit conditions. comparison of the aging of (a) PCE, (b) Fill factor, (c) Current and (d) open circuit voltage of devices prepared using HTMs, TAP-ANT-TPA (blue line), ACE-ANT-ACE (green line) and Spiro-OMeTAD (red line).

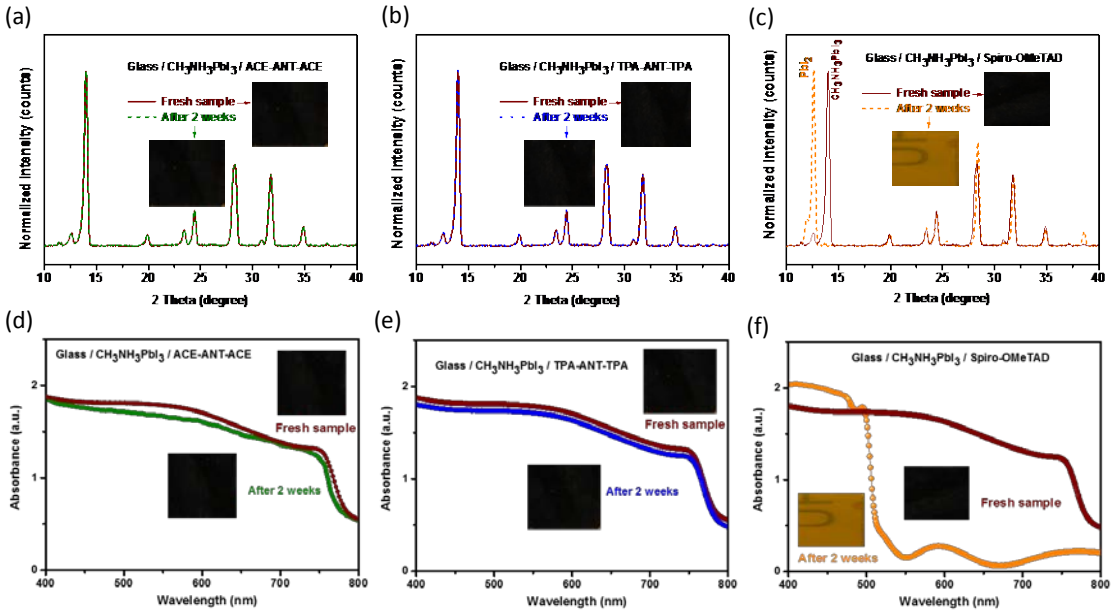

Figure S16. (a),(b),(c) XRD and (d), (e), (f) UV-visible degradation study of all three respective HTMs deposited on glass / perovskite assembly. All samples kept under continuous 1 sun illumination, in ambient air and at ~35^{o}C (sample temperature measured during illumination).

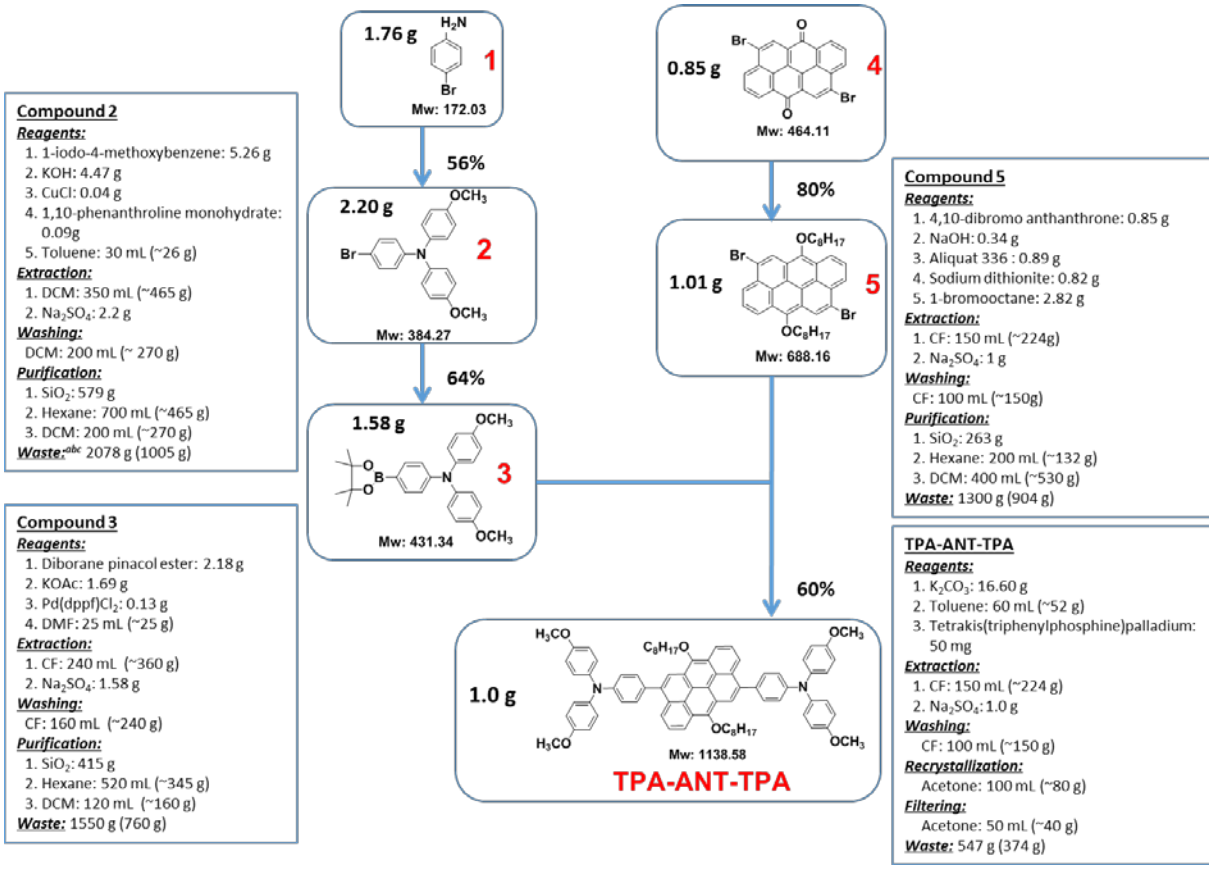

[a]Total estimated weight of chemical waste, including solvents and precipitate, for the synthesis of 1 gram of product.
[b]Total estimated weight of halogenated solvents (such as CF and DCM) is given in parentheses for the synthesis of 1 gram of product.
[c]The density of solvents (Toluene, DMF, DCM, CF, Hexane, Acetone) are referenced from Sigma-Aldrich supplier.

Figure S17. Flowchart describing the synthesis of 1g of TPA-ANT-TPA.

Table S1. Density Functional Theory (DFT) calculations of ACE-ANT-ACE and TPA-ANT-TPA.

Compound	ACE-ANT-ACE	TPA-ANT-TPA
HOMO, eV	-4.80	-4.67
LUMO, eV	-2.06	-2.04
gap, eV	2.75	2.63
VIS peak(s), nm	476	524, 467
osc strength	0.4569	0.228, 0.3535
composition	H->L 100%	H->L 85%, H-2->L 83%
PL peak(s), nm	542	633, 571, 512
osc strength	0.5789	0.0812, 0.1212, 0.5186
composition	H->L 100%	H->L 100%, H-1->L 86%, H-2->L 85%
dipole moment, D	0.16	0.17
dihedrals (counted from centre. TPA not counted)		
1	67, 71	51, 53
2	n/a	n/a

Table S2. Materials quantities and cost evaluation for the synthesis of 4-bromo-*N*,*N*-bis(4-methoxyphenyl)aniline (**2**)

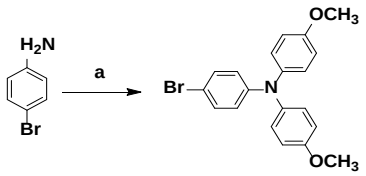

(1) (2)

Chemical Name	Weight reagent [g]	Weight solvent [mL]	Weight of workup [g or mL]	Price of chemical [AUD/g or AUD/mL]	Material Cost [AUD/g product]	Cost per step [AUD/step]
4-bromoaniline	1.76			0.32	0.57	31.91
1-iodo-4-methoxybenzene	5.26			0.65	3.40	
KOH	4.47			0.02	0.10	
CuCl	0.04			3.27	0.14	
1,10-phenanthroline monohydrate	0.09			0.78	0.07	
anhydrous Toluene		30.00		0.07	2.15	
DCM		550.00		0.01	3.41	
Na_2SO_4			2.2	0.02	0.05	
SiO_2			579	0.03	16.30	
Hexane			700	0.01	4.49	
DCM			200	0.01	1.24	

Table S3. Materials quantities and cost evaluation for the synthesis of 4-methoxy-*N*-(4-methoxyphenyl)-*N*-(4-(4,4,5,5-tetramethyl-1,3,2-dioxaborolan-2-yl)phenyl)aniline (**3**)

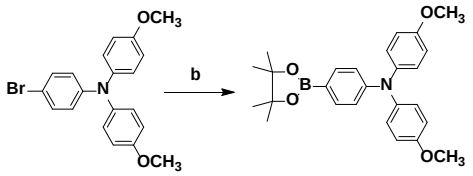

(2) (3)

Chemical Name	Weight reagent [g]	Weight solvent [mL]	Weight of workup [g or mL]	Price of chemical [AUD/g or AUD/mL]	Material Cost [AUD/g product]	Cost per step [AUD/step]
diborane pinacol ester	2.18			0.65	1.41	28.38
KOAc	1.69			0.22	0.37	
$Pd(dppf)Cl_2$	0.13			32.40	4.07	
DMF		25.00		0.15	3.78	
CF		400.00		0.01	2.96	
Na_2SO_4			1.58	0.02	0.03	
SiO2			415	0.03	11.69	
Hexane			520	0.01	3.34	
DCM			120	0.01	0.74	

Table S4. Materials quantities and cost evaluation for the synthesis of 4,10-dibromo-6,12-bis(octyloxy)anthanthrene (**5**)

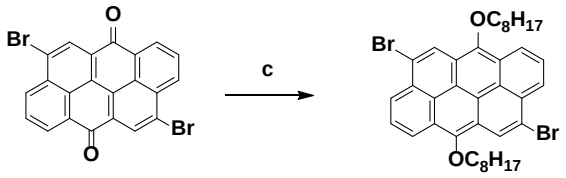

(4) **(5)**

Chemical Name	Weight reagent [g]	Weight solvent [mL]	Weight of workup [g or mL]	Price of chemical [AUD/g or AUD/mL]	Material Cost [AUD/g product]	Cost per step [AUD/step]
4,10-dibromo anthanthrone	0.85			0.21	0.18	14.51
NaOH	0.34			0.02	0.01	
Aliquat 336	0.89			0.50	0.51	
sodium dithionite	0.82			0.10	0.08	
1-bromooctane	2.82			0.25	0.70	
CF		250.00		0.01	1.85	
Na_2SO_4			1	0.02	0.02	
SiO_2			263	0.03	7.41	
Hexane			200	0.01	1.28	
DCM			400	0.01	2.48	

Table S5. Materials quantities and cost evaluation for the synthesis of 4,4'-(6,12-bis(octyloxy)-6,12-dihydronaphtho[7,8,1,2,3-*nopqr*]tetraphene-4,10-diyl)bis(*N*,*N*-bis(4-methoxyphenyl)aniline) (**TPA-ANT-TPA**)

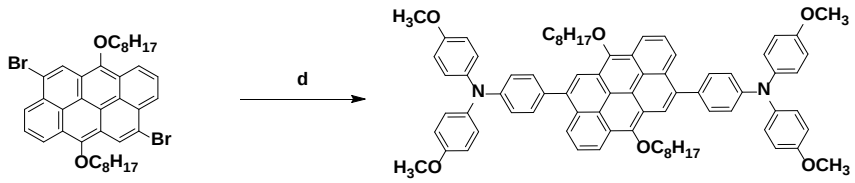

(5) **(TPA-ANT-TPA)**

Chemical Name	Weight reagent [g]	Weight solvent [mL]	Weight of workup [g or mL]	Price of chemical [AUD/g or AUD/mL]	Material Cost [AUD/g product]	Cost per step [AUD/step]
K_2CO_3	16.60			0.17	2.84	11.09
tetrakis(triphenylphosphine)palladium	0.05			24.00	1.20	
Toluene		60.00		0.07	4.29	
CF		250.00		0.01	1.85	
Na_2SO_4			1	0.02	0.02	
Acetone			150	0.01	0.89	

Total cost is ~86 AUD/g. It is equal to ~67 $/g.

Reference:

[1] S. M. Jain, Z. Qiu, L. Häggman, M. Mirmohades, M. B. Johansson, T. Edvinsson, G. Boschloo, Energy Environ. Sci. 2016, 9, 3770.

[2] S. M. Jain, B. Philippe, E. M. J. Johansson, B.-w. Park, H. Rensmo, T. Edvinsson, G. Boschloo, J. Mater. Chem. A 2016, 4, 2630.

[3] M. Planells, A. Abate, D. J. Hollman, S. D. Stranks, V. Bharti, J. Gaur, D. Mohanty, S. Chand, H. J. Snaith, N. Robertson, J. Mater. Chem. A 2013, 1, 6949.